

ORGANIC MOLECULES AND WATER IN THE INNER DISKS OF T TAURI STARS

JOHN S. CARR¹ AND JOAN R. NAJITA²

¹ Naval Research Laboratory, Code 7211, Washington, DC 20375, USA; carr@nrl.navy.mil

² National Optical Astronomy Observatory, 950 North Cherry Avenue, Tucson, AZ 85716, USA; najita@noao.edu

Received 2010 December 2; accepted 2011 March 23; published 2011 May 11

ABSTRACT

We report high signal-to-noise *Spitzer* Infrared Spectrograph spectra of a sample of 11 classical T Tauri stars. Molecular emission from rotational transitions of H₂O and OH and rovibrational bands of simple organic molecules (CO₂, HCN, C₂H₂) is common among the sources in the sample. The emission shows a range in both flux and line-to-continuum ratio for each molecule and in the flux ratios of different molecular species. The gas temperatures (200–800 K) and emitting areas we derive are consistent with the emission originating in a warm disk atmosphere in the inner planet formation region at radii <2 AU. The H₂O emission appears to form under a limited range of excitation conditions, as demonstrated by the similarity in relative strengths of H₂O features from star to star and the narrow range in derived temperature and column density. Emission from highly excited rotational levels of OH is present in all stars; the OH emission flux increases with the stellar accretion rate, and the OH/H₂O flux ratio shows a relatively small scatter. We interpret these results as evidence for OH production via FUV photodissociation of H₂O in the disk surface layers. No obvious explanation is found for the observed range in the relative emission strengths of different organic molecules or in their strength with respect to water. We put forward the possibility that these variations reflect a diversity in organic abundances due to star-to-star differences in the C/O ratio of the inner disk gas. Stars with the largest HCN/H₂O flux ratios in our sample have the largest disk masses. While larger samples are required to confirm this, we speculate that such a trend could result if higher mass disks are more efficient at planetesimal formation and sequestration of water in the outer disk, leading to enhanced C/O ratios and abundances of organic molecules in the inner disk. A comparison of our derived HCN-to-H₂O column density ratio to comets, hot cores, and outer T Tauri star disks suggests that the inner disks are chemically active.

Key words: accretion, accretion disks – circumstellar matter – infrared: stars – protoplanetary disks – stars: pre-main sequence

Online-only material: color figures

1. INTRODUCTION

Circumstellar disks around recently formed stars are the birthplaces of planets. Studies of molecules in these disks can provide insights into the planet formation process and the degree of chemical processing in disks. For example, the abundance, distribution, and evolution of water in disks are expected to have important effects on planetary system formation, including the growth of giant planets, the oxidation state of the inner disk, and the origin of water in terrestrial bodies. Protoplanetary disks could also be important sources for compounds of prebiotic interest, but the extent to which disks synthesize or preserve organic molecules is unknown. The cold gaseous component of disks at large disk radii (>40 AU) has been probed with millimeter spectroscopy (Dutrey et al. 2007). Hot molecular gas at small disk radii, including CO, H₂O, and OH, has been studied with near-infrared spectroscopy (see Najita et al. 2007a for a review). The main planet formation region of the disk, however, is found at intermediate radii and temperatures, where gas is best studied at mid- and far-infrared wavelengths. Relatively recent developments have made gas at these radii accessible to study.

Spectroscopy in the mid-infrared with the *Spitzer Space Telescope* has opened a new window on gas in the inner planet formation region of disks by the detection of water and organic molecules. Organic molecules were first detected in absorption. Lahuis et al. (2006a) reported absorption from warm (~300–700 K) HCN, C₂H₂, and CO₂ in the spectrum of the young star IRS 46. The molecular absorption is considered to originate in the inner few AU of a disk viewed close to edge-on.

Such absorption is rare (Lahuis et al. 2006a); additional examples include GV Tau (Gibb et al. 2007, 2008; Doppmann et al. 2008) and DG Tau B (Pontoppidan et al. 2008; Kruger et al. 2011).

Carr & Najita (2008) were the first to discover emission from water, OH, and organics (HCN, C₂H₂, CO₂) in *Spitzer* spectra, as reported for the T Tauri star AA Tau. The temperatures and emitting areas of the detected species were consistent with the emission arising in a temperature inversion region of the inner disk atmosphere within a few AU of the star, i.e., in the inner planet formation region of the disk. The relative column densities indicated a high abundance of water vapor in the inner disk, and comparisons to hot cores, comets, and chemical models suggested that inner disks are chemically active. Unlike disk absorption, which requires a special edge-on viewing geometry, the ability to detect molecules in emission means that organic molecules and water can potentially be studied in a large number of T Tauri disks.

Other examples of mid-infrared molecular emission in T Tauri stars were reported from subsequent analysis of existing *Spitzer* Infrared Spectrograph (IRS) data. Salyk et al. (2008) presented the detection of water and OH emission from two T Tauri disks (DR Tau and AS 205). They also described high-resolution near-infrared spectra of H₂O and OH for the same stars. The measured line velocity widths were consistent with the emission originating within a few AU of the stars, and local thermodynamic equilibrium (LTE) analysis indicated large columns of warm gas. Pascucci et al. (2009) reported HCN and C₂H₂ emission from several T Tauri stars, based on spectra taken in the

Report Documentation Page		<i>Form Approved OMB No. 0704-0188</i>
<p>Public reporting burden for the collection of information is estimated to average 1 hour per response, including the time for reviewing instructions, searching existing data sources, gathering and maintaining the data needed, and completing and reviewing the collection of information. Send comments regarding this burden estimate or any other aspect of this collection of information, including suggestions for reducing this burden, to Washington Headquarters Services, Directorate for Information Operations and Reports, 1215 Jefferson Davis Highway, Suite 1204, Arlington VA 22202-4302. Respondents should be aware that notwithstanding any other provision of law, no person shall be subject to a penalty for failing to comply with a collection of information if it does not display a currently valid OMB control number.</p>		
1. REPORT DATE DEC 2010	2. REPORT TYPE	3. DATES COVERED 00-00-2010 to 00-00-2010
4. TITLE AND SUBTITLE Organic Molecules and Water in the Inner Disks of T Tauri Stars		5a. CONTRACT NUMBER
		5b. GRANT NUMBER
		5c. PROGRAM ELEMENT NUMBER
6. AUTHOR(S)		5d. PROJECT NUMBER
		5e. TASK NUMBER
		5f. WORK UNIT NUMBER
7. PERFORMING ORGANIZATION NAME(S) AND ADDRESS(ES) Naval Research Laboratory, Code 7211, Washington, DC, 20375		8. PERFORMING ORGANIZATION REPORT NUMBER
9. SPONSORING/MONITORING AGENCY NAME(S) AND ADDRESS(ES)		10. SPONSOR/MONITOR'S ACRONYM(S)
		11. SPONSOR/MONITOR'S REPORT NUMBER(S)
12. DISTRIBUTION/AVAILABILITY STATEMENT Approved for public release; distribution unlimited		
13. SUPPLEMENTARY NOTES		
14. ABSTRACT <p>We report high signal-to-noise Spitzer Infrared Spectrograph spectra of a sample of 11 classical T Tauri stars. Molecular emission from rotational transitions of H₂O and OH and rovibrational bands of simple organic molecules (CO₂, HCN, C₂H₂) is common among the sources in the sample. The emission shows a range in both flux and line-to-continuum ratio for each molecule and in the flux ratios of different molecular species. The gas temperatures (200?800 K) and emitting areas we derive are consistent with the emission originating in a warm disk atmosphere in the inner planet formation region at radii <2 AU. The H₂O emission appears to form under a limited range of excitation conditions, as demonstrated by the similarity in relative strengths of H₂O features from star to star and the narrow range in derived temperature and column density. Emission from highly excited rotational levels of OH is present in all stars; the OH emission flux increases with the stellar accretion rate, and the OH/H₂O flux ratio shows a relatively small scatter. We interpret these results as evidence for OH production via FUV photodissociation of H₂O in the disk surface layers. No obvious explanation is found for the observed range in the relative emission strengths of different organic molecules or in their strength with respect to water. We put forward the possibility that these variations reflect a diversity in organic abundances due to star-to-star differences in the C/O ratio of the inner disk gas. Stars with the largest HCN/H₂O flux ratios in our sample have the largest disk masses. While larger samples are required to confirm this, we speculate that such a trend could result if higher mass disks are more efficient at planetesimal formation and sequestration of water in the outer disk, leading to enhanced C/O ratios and abundances of organic molecules in the inner disk. A comparison of our derived HCN-to-H₂O column density ratio to comets, hot cores, and outer T Tauri star disks suggests that the inner disks are chemically active.</p>		
15. SUBJECT TERMS		

16. SECURITY CLASSIFICATION OF:			17. LIMITATION OF ABSTRACT Same as Report (SAR)	18. NUMBER OF PAGES 18	19a. NAME OF RESPONSIBLE PERSON
a. REPORT unclassified	b. ABSTRACT unclassified	c. THIS PAGE unclassified			

Standard Form 298 (Rev. 8-98)
Prescribed by ANSI Std Z39-18

Table 1
Observations and Sample Parameters

Object	Frame Time ^a (s)	Cycles ^b	Flux ^c (Jy)	SpT	$\log M_{\text{acc}} (M_{\odot} \text{ yr}^{-1})$	Disk Mass ($\log M_{\odot}$)
AA Tau	31.5	24	0.32	K7	-8.5	-1.89
BP Tau	31.5	24	0.37	K7	-7.5	-1.74
DG Tau	6.3	24	5.25	K7	-6.3	-1.62
DK Tau ^d	31.5	16	0.75	K7	-7.4	-2.32
DO Tau	31.5	16	2.00	M0	-6.8	-2.15
GI Tau	31.5	8	0.75	K6	-8.0	...
GK Tau	31.5	8	0.79	K7	-8.2	-2.80
RW Aur ^d	6.3	26	1.48	K3	-7.1	-2.44
UY Aur ^e	6.3	20	2.66	K7	-7.2	-2.74
AS353A	31.5	16	1.15	K5	-6.3	...
V1331Cyg	31.5	16	1.06	C	-6.1	...

Notes.

^a Total SH integration time on source = $2 \times (\text{Frame Time}) \times \text{Cycles}$.

^b Number of on-source cycles. Number of cycles in off position is 1/2 that on-source, except for GI Tau and GK Tau, where the on and off source cycles are equal.

^c Continuum flux at 14 μm measured in this work.

^d Unresolved binary within the IRS slit, with secondary contributing <10% of the broadband mid-infrared flux.

^e UY Aur is an unresolved binary within the IRS slit with both components contributing similar amounts to the broadband mid-infrared flux.

low-resolution mode of *Spitzer* IRS. They also presented observations of young brown dwarfs and the first detections of C₂H₂ emission from their disks.

Studies of larger samples of young stars have fully established that mid-infrared emission from water and other molecules is a common property of T Tauri stars. Pontoppidan et al. (2010b) presented a search for molecular emission in 73 stars. The sample included T Tauri stars in Chamaeleon, Ophiuchus, and Lupus that are part of a dedicated *Spitzer* cycle-5 program on molecular emission (PID 50641; PI: J. Carr), re-processed spectra from the c2d Legacy program (Evans et al. 2003), and archival spectra of Herbig Ae/Be stars. Emission from H₂O, HCN, CO₂, C₂H₂, and OH is shown to be widespread among the T Tauri stars. On the other hand, the Herbig Ae/Be stars lack detectable molecular emission, with upper limits on line/continuum ratios 3–10 times lower than measured in T Tauri stars. However, hints of H₂O/OH emission are seen in the spectra of some Herbig Ae/Be stars and one shows CO₂ emission. Detailed analysis of this sample of stars is presented in Salyk et al. (2011).

In this paper, we analyze in detail high-quality *Spitzer* spectra of a sample of 11 T Tauri stars. These stars constitute the initial cycle-2 *Spitzer* program that carried out a deep search for H₂O and other gas emission lines in T Tauri stars, which included the observations of AA Tau reported in Carr & Najita (2008). A simple LTE slab model is used to decompose the spectra into contributions from water and organics and determine the emitting gas properties for each molecular species. We describe the characteristics and discuss the origins of the molecular emission. Ratios of our derived molecular column densities are used as estimates of relative abundances to compare to results for hot cores, comets, outer T Tauri disks and protostellar envelopes, and chemical models of disk atmospheres.

2. OBSERVATIONS

2.1. *Spitzer* IRS Spectroscopy

The mid-infrared spectra presented here were obtained with the *Spitzer* IRS (Houck et al. 2004) using the short-high (SH; 10–19 μm) module, with a nominal resolving power of ~ 600 .

All spectra were obtained in staring mode, which places the target at two nod positions along the length of the 11" \times 4.7" slit. The total integration times were set using the spectroscopy performance estimation tool to achieve a continuum signal-to-noise ratio (S/N) ≥ 300 , using 8–24 nod cycles. The redundancy provided by the large number of cycles enabled the evaluation of the noise statistics and identification of badly behaved pixels. The SH frame time and number of cycles for each target are given in Table 1. Dedicated background observations were obtained for all targets at off positions clean of continuum sources or known nebulosity. In most cases, the background integration time was one-half of the time spent on the target.

The T Tauri stars studied in this paper were observed in *Spitzer* GO program 2300. These observations were designed primarily to search for H₂O emission from disks, before such emission was known to be common among T Tauri stars. Results from this program for AA Tau were first reported in Carr & Najita (2008). The program also obtained spectra for all targets in the long–high (LH; 19–37 μm) module; analyses of those data will be presented in a future paper.

The main part of this sample has nine well-studied classical T Tauri stars in the Taurus-Auriga star-forming region, selected to cover a range in mass accretion rate. Spectral types range from K3 to M0. The program included two additional sources, AS353A and V1331 Cyg, both of which are extremely active stars known to have CO overtone, H₂O, or OH emission in the near-infrared (Najita et al. 2007a, 2009; Doppmann et al. 2011; Prato et al. 2003). V1331 Cyg is often presumed to have a spectral type and mass intermediate between T Tauri stars and Herbig Ae stars due to the non-detection of photospheric features and a higher luminosity than typical T Tauri stars (e.g., Hamann & Persson 1992). Of the Taurus sources, DG Tau has also shown CO overtone and near-infrared water emission (Carr 1989; Najita et al. 2000), but the CO overtone emission varies and is not always present (Greene & Lada 1996; Biscaya et al. 1997). V1331 Cyg, AS353A, and DG Tau also have known jets and/or outflows.

The star UY Aur is a 0.9" binary whose components have similar accretion rates (Hartigan & Kenyon 2003) and comparable brightness in the infrared; the binary flux ratio at 10 μm has

varied from 1.2 to 2.0 over a decade (Skemer et al. 2010). The $10\text{ }\mu\text{m}$ silicate spectra of the components have been spatially resolved by Skemer et al. (2010). However, we cannot determine the contribution of the components to the line emission spectrum in the unresolved *Spitzer* IRS spectra. Two other stars have companions within the SH slit, DK Tau, and RW Aur, with separations of $2''.4$ and $1''.4$, respectively. The primary dominates the mid-infrared flux in each case, with flux ratios ~ 10 (McCabe et al. 2006).

Some properties of the sample that are used in plots later in this paper are listed in Table 1. The stellar accretion rates for most stars are those reported in Najita et al. (2007b), which placed accretion rates from different literature sources on the same scale as Gullbring et al. (1998). Accretion rates are probably no better than a few tenths of a dex due to intrinsic variability. For GI Tau, we adopted the accretion rate from Hartmann et al. (1998), which is on the same scale as Gullbring et al. We scaled down the accretion rate for AS353A (Hartigan et al. 1995) by 0.12, based on the prescription of Najita et al. (2007b). We also made a rough estimate of the accretion rate of V1331 Cyg based on the accretion flux derived by Eisner et al. (2007). Assuming a distance of 550 pc (as in Najita et al. 2009), the corresponding accretion rate is $\sim 10^{-6} M_{\odot} \text{ yr}^{-1}$. The disk masses are from the submillimeter measurements in Andrews & Williams (2005).

2.2. Data Reduction

The stars in the sample are sufficiently bright that systematic effects become the limiting factor in the achievable S/N. Therefore, the data processing procedures are critical in maximizing the quality of the spectra. Our procedures were initially described in Carr & Najita (2008), and we cover these in more detail here. The data processing was carried out using a combination of standard IRAF tasks and custom routines.

We begin with the non-flat-fielded “droop” images, multiplied by the frame time. For each target, frames are combined to form a mean image for the “A” slit position, the “B” slit position, and the combined background positions. When combining frames, the noise is calculated for each pixel and any highly deviant values are rejected. In addition, pixels in the background image that have a standard deviation much higher than the distribution for all pixels are flagged as being unstable; these are similar to the original definition for “rogue pixels” for the IRS arrays. These flagged pixels are used to make an unstable pixel mask, which is combined with known permanently dead pixels for a total bad pixel mask. The mean background image is then subtracted from the mean A and B images, which remove any background signal, dark current, and hot (but stable) pixels. These images are next divided by a flat field. We use the pipeline flat field that has been normalized in both the spectral and spatial dimensions using the IRAF task `apflatten`. This avoids artificial increases in the noise where the flat drops quickly near the ends of the slit and preserves the noise statistics. After division by the flat field, the bad pixel mask is applied, replacing bad pixels by interpolation in the spectral direction. A visual inspection is also carried out and any missed and obviously bad pixels are fixed by hand. The multi-order spectra are traced and extracted with optimal weighting using the IRAF task `apall`, making use of the noise statistics determined from the data. The wavelength scale for the extracted spectra was obtained by fitting a polynomial function to the pipeline wavelength calibration table.

The extracted orders were divided by a spectral response function to remove the instrumental spectral shape and fringing

and to flux calibrate the spectra. The spectral response function was customized for each slit position of each target using a suite of spectra for the IRS standard stars ξ Dra and δ Dra. These data were obtained from the *Spitzer* archive and processed in the same way as the target spectra, with an additional step of dividing the spectra by a corresponding model template provided on the *Spitzer* IRS Web site. The quality of fringe correction is very sensitive to the choice of spectrum in the suite of calibrators; most likely this is due to small differences in centering of stars in the slit. We divided the target spectrum by each of the calibrator spectra to find those that minimized the residual fringing. For the SH module, we examined order 20, which usually shows the largest residual fringing and showed few intrinsic emission features in the T Tauri stars. Those standard star spectra (typically 1–4) that gave the smallest residual fringing for a target and slit position were averaged for the spectral response function. Standard star spectra that minimized the residual fringing also eliminated significant curvature in the divided spectra at the ends of the orders.

While this procedure provides a good correction for fringing in our sample of stars, there is often some residual fringing seen in the highest (shortest wavelength) orders. To correct for this remaining residual we used the routine `IRSFRINGE` (Lahuis et al. 2006b) to search for and remove any significant fringes near the main fringe frequencies of 3500 and 7800 cycles. However, no correction was applied for the 3500 cycle fringe in orders near the HCN and C_2H_2 bands, because the *R*- and *P*-branch spacing for these molecules is close to this frequency.

Finally, the individual spectral orders were combined using appropriate weighting in the wavelength overlap regions. No scaling of individual orders was required because the match in flux levels between adjacent orders was excellent. The A and B spectra were then averaged. A comparison of the A and B spectra was used to estimate the noise in the mean spectrum. The continuum S/N at $14\text{ }\mu\text{m}$ ranged from 200 to 400.

3. OBSERVED SPECTRA

The complete SH spectra are presented in Figure 1. The low-frequency variations in the continuum are due to dust emission features, in particular the amorphous silicate bands centered at 10 and $18\text{ }\mu\text{m}$. Crystalline silicates are present in many objects, with forsterite emission centered at $11.2\text{ }\mu\text{m}$, $16\text{ }\mu\text{m}$, and $11.9\text{ }\mu\text{m}$, and silica emission near $12.5\text{ }\mu\text{m}$. We also find weak and shallow emission features centered roughly at 13.7 , 14.5 , and (less discernible) $15.5\text{ }\mu\text{m}$ that sometimes underlay the forest of emission lines. These peaks correspond to wavelengths of pyroxenes (Jaeger et al. 1998; Chihara et al. 2002), but curiously the corresponding peaks of the $10\text{ }\mu\text{m}$ complex are not apparent in the spectra. No broadband absorption features are identified in the spectra.

As was described by Carr & Najita (2008), rotational lines of H_2O dominate the forest of emission lines seen above the dust continuum. Some of the rotational transitions that make up the water emission features are identified in Figure 4 of Pontoppidan et al. (2010b). Relative to the continuum, the water emission ranges from very prominent (e.g., RW Aur) to barely discernable (e.g., DO Tau). Water emission is not detected in three stars: DG Tau, V1331 Cyg, and AS 353A. The other molecules contributing to the emission spectrum are rotational transitions of OH and the rovibrational fundamental bending modes of HCN (ν_2), C_2H_2 (ν_5), and CO_2 (ν_2), with *Q*-branches at 14.0 , 13.7 , and $14.97\text{ }\mu\text{m}$, respectively.

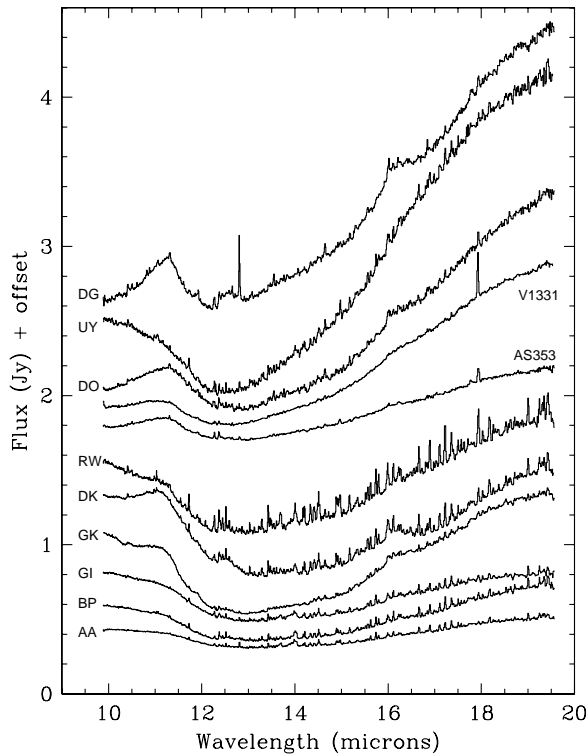


Figure 1. *Spitzer* SH IRS spectra for the entire sample. For the purpose of plotting, offsets have been applied to the spectra of several stars. The offsets in Jy are -0.25 for GI Tau, -0.20 for GK Tau, $+0.05$ for DK Tau, -0.35 for RW Aur, -0.40 for UY Aur, $+0.85$ for V1331 Cyg, and $+0.60$ for AS 353A. For DG Tau, the spectrum was also divided by a linear function in order to reduce the spectral slope and allow plotting on the same figure; hence, the relative line fluxes and the spectral slope across the SH band are reduced by nearly a factor of two from the true spectrum for DG Tau.

A continuum was subtracted from each spectrum in order to facilitate modeling and measurement of the emission features. The definition of the continuum is challenging because there are few true continuum regions due to the density of emission lines and the low spectral resolution. This is further complicated by the presence of the dust emission features, which increases the uncertainty in the continuum level for water lines near 12.5 , 14.5 , and 16 μm . In addition, the HCN and C_2H_2 bands overlay the wide and shallow 13.7 μm dust feature. We used our spectral modeling (Section 4) to provide a guide to the best continuum or pseudo-continuum regions. Polynomials were fit for 6 – 8 separate intervals over the SH range, and these individual continuum-subtracted regions were joined into a final spectrum. All the continuum-subtracted spectra are presented in Figure 2 for the 12 – 16 μm region, which contains the organic molecular bands.

The complexity of the molecular spectrum in this region is demonstrated in Figure 3, which shows synthetic emission spectra for the individual molecules calculated using the methods described in Section 4. Figure 3(a) shows that there is significant blending of the molecular emission from different species at the resolution of the IRS SH module. Failure to account for this blending can lead to erroneous fluxes or false detections for a molecule, depending on the relative emission strength of different species. Furthermore, nearly all observed molecular features are blends of individual rotational or rovibrational transitions (compare to Figure 3(b), the same model at high resolution).

Emission from OH is detected from every star in the sample, including those in which H_2O emission is not detected. The most isolated and easily measured OH feature is at 14.64 μm

(see Figure 2). This feature is a blend of unresolved components of the ground vibrational state with total angular momentum quantum number $N = 19$. Other rotational OH emission features, ranging from $N = 14$ to as high as $N = 29$, can be seen in the spectra over the SH spectral range (see Najita et al. 2010 for a list of OH wavelengths in this spectral region).

Prominent HCN emission is clearly present in five stars of the sample (including the previously reported case of AA Tau). HCN emission may be present in UY Aur, but our modeling (Section 4) shows that a large part of the 14.0 μm feature in UY Aur is due to H_2O and OH. C_2H_2 emission is present in at least three of these stars, but modeling is required to account for the H_2O and HCN emission in the 13.7 μm feature in others.

The most commonly observed organic molecule is CO_2 . It is detected in all stars except DG Tau, with a questionable detection in DO Tau. CO_2 is observed in some stars without HCN or C_2H_2 emission and in two that lack H_2O emission (V1331 Cyg and AS 353A). Other stars showing only CO_2 emission were reported by Pontoppidan et al. (2010b). Note that a pair of H_2O emission features is blended with the blue wing of the CO_2 Q -branch (see Figure 2).

Najita et al. (2010) reported the identification of a Q -branch of HCO^+ at 12.06 μm in the *Spitzer* spectrum of the transitional disk object TW Hya. We do not detect this HCO^+ band in any star in our sample of T Tauri stars. HCO^+ emission with the distance-corrected flux measured in TW Hya would likely have escaped detection in our sample of Taurus objects, especially since the HCO^+ Q -branch is close to an observed water feature at 12.08 μm . The detection of HCO^+ emission from TW Hya was simplified by the notable lack of strong water emission.

One notable result is that the relative intensities of different molecular species differ from object to object. The spectra in Figure 2 show that the flux ratios of organic molecules to water, and the flux ratios of different organic bands, are not constant. Compare, for example, the relative strength of CO_2 to HCN in UY Aur and BP Tau, or the relative strength of HCN-to-water lines near 14.4 μm in AA Tau and GK Tau. We return to this point in Section 5, where we make use of representative flux measurements for the emission from each molecule.

There are also some atomic emission lines observed in the SH spectra. The $[\text{Ne II}]$ line at 12.81 μm is very common in this sample, but it is often quite weak and is close in wavelength to a number of weak molecular lines. It appears most prominently in AA Tau, UY Aur, and DG Tau. Atomic hydrogen has a number of transitions in this wavelength region (see Najita et al. 2010), with the strongest line at 12.37 μm line. However, this line is partially blended with H_2O emission features. The 17.93 μm line of $[\text{Fe II}]$ is the most prominent emission line in V1331 Cyg and AS353A and is also present in DG Tau. In other stars, this $[\text{Fe II}]$ line is coincident with a water-emission feature.

4. SYNTHETIC SPECTRA

4.1. Modeling Method

Following the methods in Carr & Najita (2008), we calculated synthetic spectra of the detected molecular species in order to place constraints on the gas conditions producing the emission. This approach adopts a plane parallel slab model with a single temperature and column density for each molecule and assumes that all level populations are in LTE. The three variables required to fit the spectrum for a particular molecule are the temperature T , the line-of-sight (LOS) column density N of the molecule, and the projected emitting area. We define R_e as the radius

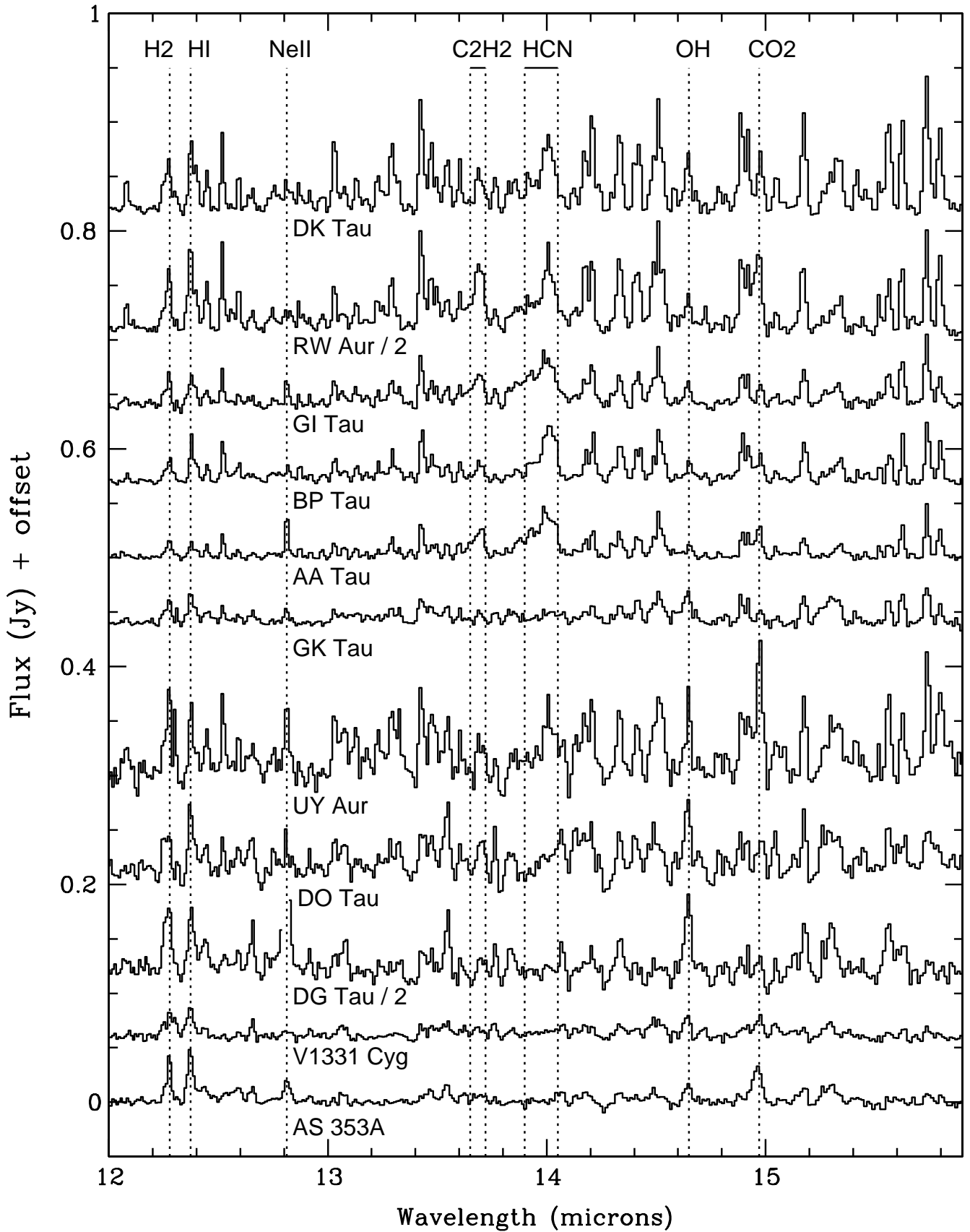


Figure 2. SH spectra in the 12–16 μm region after subtraction of the continuum. The spectra for RW Aur and DG Tau have been divided by 2. The wavelength positions are indicated for the Q -branches of HCN, C₂H₂, and CO₂, the $S(2)$ rotational transition of H₂, the 12.37 μm line of H₁, the 12.81 μm [Ne II] line, and the 14.64 μm rotational feature of OH. The remaining emission features are mostly due to rotational transitions of H₂O with some additional OH features.

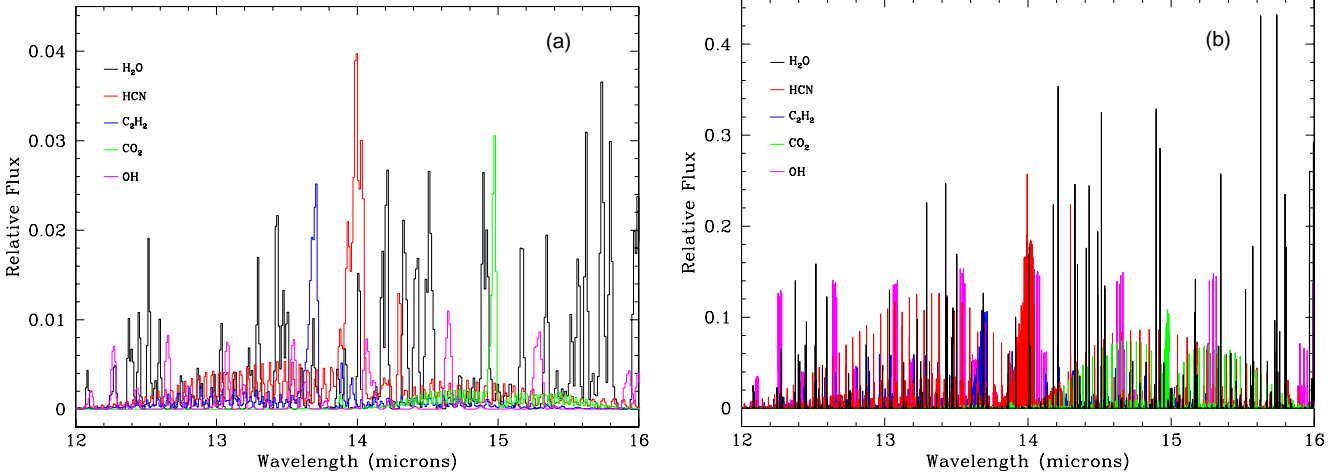


Figure 3. Synthetic spectrum for the 12–16 μm region, showing the individual contributions from each of the detected molecules. The temperatures, column densities, and areas are characteristic of those derived for T Tauri stars in this paper. The H₂O spectrum is plotted as a black histogram, HCN as red, C₂H₂ as blue, CO₂ as green, and OH as magenta. (a) For the resolution and sampling of the IRS SH module. (b) For a resolving power of $R = 30,000$. The H₂O flux was divided by 3 in order to display it adequately with respect to the other molecules.

(A color version of this figure is available in the online journal.)

of a circular region with this emitting area. The temperature and column density are determined by matching the relative strengths of spectral features (usually blends of lines) in the case of H₂O and OH, or by fitting the shape of the Q -branch in the case of HCN, C₂H₂, and CO₂. For each combination of temperature and column density, R_e is adjusted to match the observed absolute flux. We neglect continuum dust opacity within the line-emitting layer. The local line width was taken to be due to thermal broadening without assuming any additional turbulent motions. The synthetic spectrum was first calculated at a resolution sufficient to sample the local line width and then smoothed to the resolution of IRS. The result was binned to the same wavelength sampling as the observed spectra to allow easy direct comparison.

The molecular line data are taken from the HITRAN database (Rothman et al. 2005), with the exception of HCN. For HCN, we used a theoretical line list from Harris et al. (2006), which includes higher vibrational bands than are present in the HITRAN line list. The Harris et al. line strengths must be increased by a factor of six to account for the state-independent degeneracy factor (Fischer et al. 2003) as used in the HITRAN database and its associated partition functions. Because the calculated line strengths from Harris et al. are somewhat larger than the corresponding ones in HITRAN, we further scaled them by a factor of 0.88 in order to be consistent with synthetic spectra that use the HITRAN data for HCN. For H₂O, we also ran models with the BT2 line list (Barber et al. 2006). We found no significant differences between spectra computed with the BT2 and HITRAN line lists for the range of temperatures that fit the IRS water spectra. However, we caution that the HITRAN line list will be inadequate at significantly higher (>1000 K) temperatures. The partition functions were calculated using available FORTRAN routines from the work of Fischer et al. (2003), which are consistent with the definition of statistical weights in the HITRAN database.

4.1.1. H₂O and OH

In modeling the water emission, we focused on obtaining the best fit to the H₂O spectrum in the 12–16 μm region. The energy levels for the H₂O transitions have no overall trend with wavelength and the lines in the 12–16 μm interval

Table 2
Results for H₂O Modeling

Object	T (K)	$N(\text{H}_2\text{O})^a$ (10^{16} cm^{-2})	R_e^b (AU)
AA Tau	575 (50)	78 (20)	0.85 (0.12)
BP Tau	650 (50)	78 (20)	0.83 (0.09)
DK Tau	650 (50)	60 (12)	1.27 (0.15)
GI Tau	575 (50)	42 (12)	1.16 (0.20)
RW Aur	600 (80)	155 (37)	1.49 (0.24)
UY Aur	600 (100)	179 (119)	1.04 (0.45)

Notes.

^a LOS column density.

^b Radius of projected emitting area.

are representative of the range of upper energy levels within the wavelength coverage of the IRS. In our experience, this approach provides a reasonable characterization of the average water emission properties in the full *Spitzer* spectrum (but see Section 4.2.2). By focusing on this wavelength region we can also optimize the removal of the water emission spectrum in the region of the organic emission bands, which aids in modeling these features. We also fit and remove an OH emission spectrum for the same purpose.

Synthetic H₂O spectra were calculated over a range in temperature and column density and compared to the observed spectrum. The final H₂O model parameters were based on a best fit by eye to the spectrum. The approach used for the organic bands in Section 4.1.2, of calculating χ^2 from the difference of the model and observed spectrum, did not work as well over the large wavelength interval for H₂O; variations in the zero continuum level and intervals with weak or no lines had undue influence on the fit. Table 2 gives the model parameters adopted for H₂O. An example synthetic spectrum is overplotted on the observed spectrum of BP Tau in Figure 4. For GK Tau and DO Tau, H₂O is detected but the S/N in the emission lines is insufficient to constrain the parameters well. For the purpose of subtracting a synthetic H₂O spectrum from the data for these two stars, scaled synthetic spectra were calculated using the mean temperature and column density in Table 2.

Emission from high rotational transitions of OH is present throughout the SH spectral region in all of the stars in our sample.

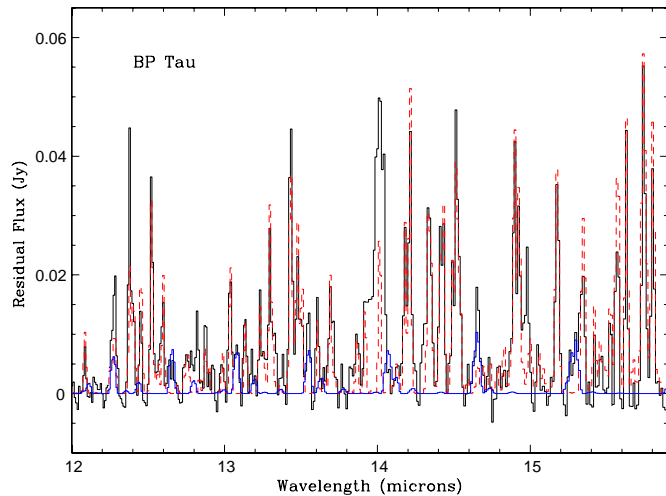


Figure 4. Synthetic H_2O model spectrum for BP Tau (dashed red line) overplotted on the observed continuum-subtracted spectrum. The model parameters are given in Table 2. The solid bold (blue) line shows the model OH spectrum used for BP Tau.

(A color version of this figure is available in the online journal.)

After subtraction of the synthetic H_2O spectrum, a model OH spectrum was calculated to match the OH spectrum (see Figure 4 for an example). We subtract this OH synthetic spectrum from the data, though the only feature that has some impact on our results is the OH feature at $14.06\ \mu\text{m}$ ($N = 20$), which blends with the red wing of the HCN band (see Figure 3).

4.1.2. The Organics: HCN, C_2H_2 , and CO_2

In modeling the HCN, C_2H_2 , and CO_2 bands, we first subtract the best $\text{H}_2\text{O} + \text{OH}$ model for each object from the observed spectrum. H_2O can contribute significantly to the flux within the Q -branches of HCN and C_2H_2 . In addition, both HCN and C_2H_2 contribute emission to the Q -branch of the other, which can be important when the emission from one molecule is significantly greater than the other. BP Tau is a good example where this blending produces an apparent C_2H_2 feature. As can be seen in Figure 4, BP Tau shows emission near $13.7\ \mu\text{m}$ that could be mistaken for the C_2H_2 band; however, the model in Figure 4 shows that H_2O emission accounts for most of this flux. Further modeling shows HCN emission can account for the remaining residual.

The shapes of the Q -branches are determined by both temperature and column density. Synthetic spectra were calculated on a grid in T and N , scaling R_e to match the model flux to the observed flux integrated over the band. χ^2 was calculated at each grid point from the difference of the model and observed spectrum, and contour plots of χ^2 were produced to determine the best-fit values and confidence intervals. There is significant degeneracy between T and N in fitting each of the three molecular bands, with increasing T offset by decreasing N .

When calculating the grid of HCN models, a synthetic C_2H_2 spectrum was subtracted from the observed spectrum to account for C_2H_2 contribution to the HCN band. This fixed C_2H_2 model spectrum was calculated from a combined HCN and C_2H_2 model that was close to the final solution based on a first round of fitting. Two examples of contour plots of χ^2 for HCN are shown in Figure 5. The heavy contour is the 90% confidence limit, which we adopt as the uncertainty range.

A similar procedure was followed for fitting the CO_2 Q -branch. Before fitting the CO_2 band, both the best $\text{H}_2\text{O} + \text{OH}$

model and the final $\text{HCN} + \text{C}_2\text{H}_2$ model were subtracted from the data. Example χ^2 contour plots for CO_2 are shown in Figure 6.

For C_2H_2 , we assumed that HCN and C_2H_2 have the same excitation temperature and emitting area, and adjusted the C_2H_2 abundance relative to HCN to fit the C_2H_2 band. The reason for this approach is that T and N were not generally constrained at a useful level of confidence, probably because of the lower flux in the C_2H_2 Q -branch and greater contamination from H_2O and HCN. An exception is RW Aur, which has the largest C_2H_2 -to-HCN flux ratio in the sample (see Section 4.2.1).

4.2. Modeling Results

4.2.1. Organic Emission

The best-fit (minimum χ^2) synthetic spectra for HCN and C_2H_2 are shown in Figure 7, overplotted on the observed spectra with the best $\text{H}_2\text{O} + \text{OH}$ model subtracted. In some cases (e.g., DK Tau), significant residuals remain after fitting the $\text{HCN} + \text{C}_2\text{H}_2$ model; many of these residuals coincide with H_2O features that are not well matched by the best-fit water spectrum. We were able to determine HCN parameters (Table 3) for five of the six stars in which HCN was detected. For UY Aur, the HCN band is only marginally detected (Figure 7), but its measured strength is sensitive to the choice of the continuum fit. Emission from C_2H_2 in UY Aur can only be considered as an upper limit.

The observed HCN Q -branches are a blend of multiple rovibrational bands, with significant contribution to the emission from vibrational levels up to $v = 3$ or 4 (depending on the temperature) and rotational levels up to $J = 24$ –30. In the best cases (AA Tau and BP Tau in Figure 7), the R -branch lines can be discerned extending to shorter wavelengths to at least the $J = 22$ –21 transition. Hence, HCN is both rotationally and vibrationally hot, and the fits in Figure 7 are consistent with a similar rotational and vibrational excitation temperature. A possible exception is GI Tau, which shows an excess at $13.85\ \mu\text{m}$ relative to the model. This could be excess emission from the $v = 4$ and 5 vibrational bands, but an unidentified spectral feature is also a possibility. The definition of the continuum is also an issue at this spectral resolution and wavelength, especially since HCN and C_2H_2 sit atop the $13.7\ \mu\text{m}$ solid-state feature which has an unknown spectral structure.

The best-fit model for the HCN band is always optically thick or marginally optically thick, with $\tau = 0.4$ –4 in the $Q(10)$ line of the $v = 1$ –0 band. The HCN column densities for the five stars have a range of about three, with temperatures between 550 and 850 K. The contour plots in Figure 5 show that as the temperature is decreased (or increased) a respective increase (or decrease) in the column density can produce acceptably good fits over a range in parameters. Within the 90% confidence interval, the lower limit on the temperature corresponds to the upper limit on the column density; these parameters are given in Table 3 as the “Optically Thick” solution. The upper limits on the HCN column densities are 2–5 times greater than the minimum χ^2 solution.

For each object there also exists a warmer, optically thin solution within the 90% confidence interval. This is where the contours in Figure 5 continue to lower column density at roughly constant temperature. Hence, while the fits place an upper limit on the temperature that corresponds to the optically thin case, there is no formal lower limit on the column density, as long as an arbitrarily large area (but constant number of molecules) can be invoked to produce the total emission flux. A lower limit can

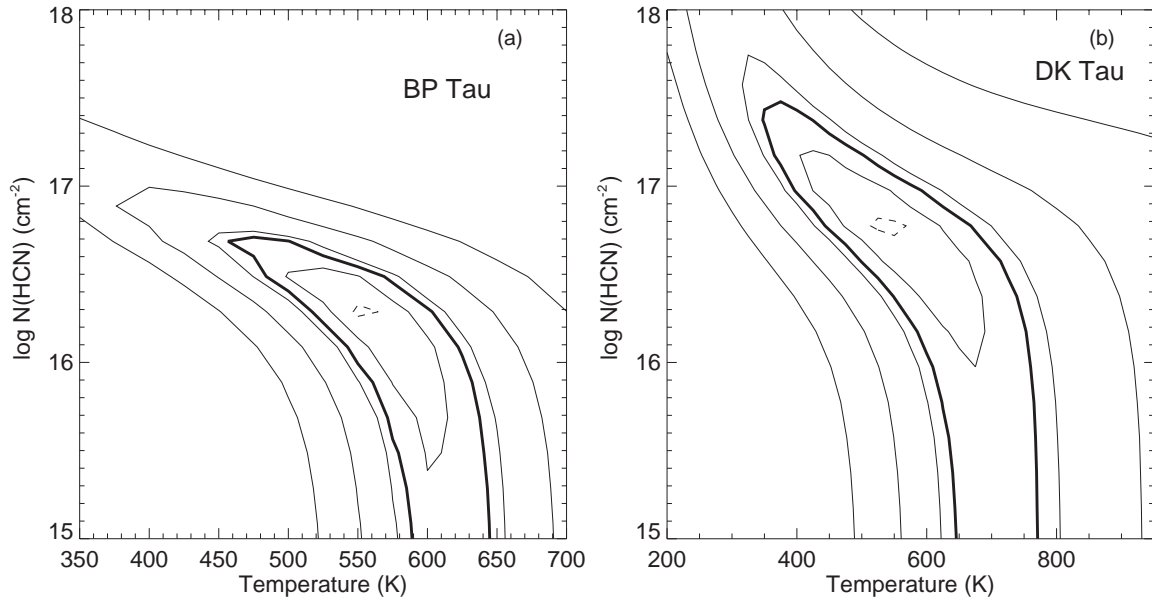


Figure 5. Contour plots of χ^2 as a function of $N(\text{HCN})$ and T for fits to the HCN Q -branch in BP Tau and DK Tau. The bold line is the 90% confidence contour, the dashed line indicates the location of minimum χ^2 , and the thin solid lines correspond to 1σ , 2σ , 3σ , and 4σ .

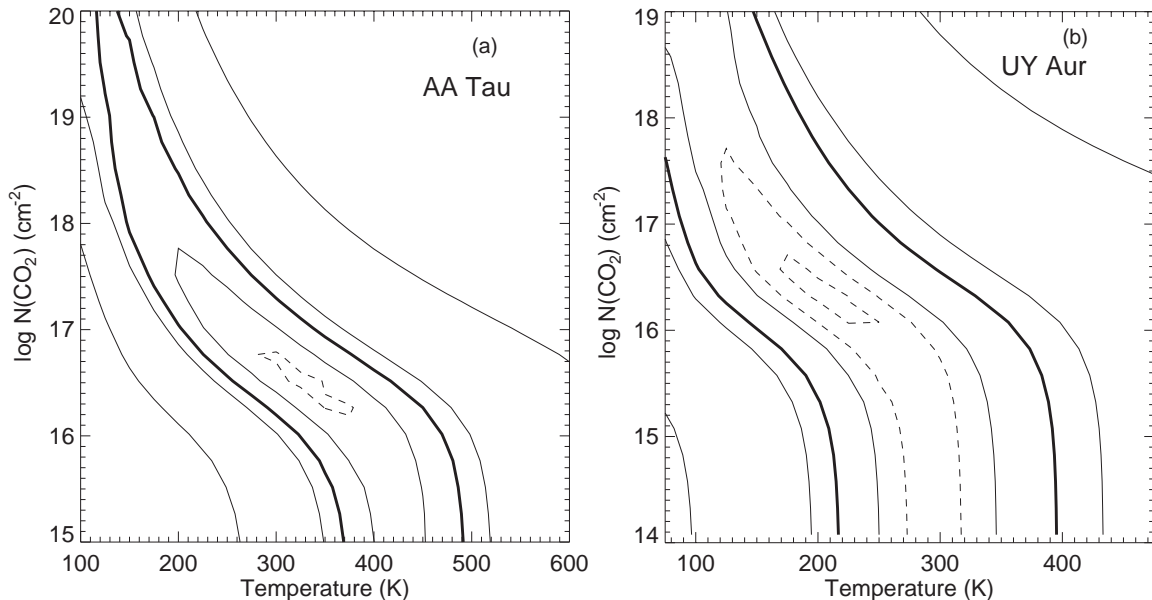


Figure 6. Contour plots of χ^2 as a function of $N(\text{CO}_2)$ and T for fits to the CO_2 Q -branch in AA Tau and UY Aur. The bold line is the 90% confidence contour, the dashed line indicates the location of minimum χ^2 , and the thin solid lines correspond to 1σ , 2σ , and 3σ .

Table 3
Results for HCN Modeling

Object	Best Fit ^a			Optically Thick ^b			Optically Thin ^c	
	T (K)	$N(\text{HCN})$ (10^{16} cm^{-2})	R_e (AU)	T (K)	$N(\text{HCN})$ (10^{16} cm^{-2})	R_e (AU)	T (K)	$N(\text{HCN})$ (10^{16} cm^{-2})
AA Tau	690	6.5	0.28	570	13.0	0.28	840	0.41
BP Tau	550	2.2	0.50	490	5.1	0.47	605	0.56
DK Tau	540	6.0	0.37	350	31.0	0.54	705	0.20
GI Tau	850	1.8	0.42	680	8.4	0.27	890	0.22
RW Aur	690	2.1	0.59	500	8.6	0.51	745	0.27

Notes. Column densities are LOS, and radii are that of the projected emitting area.

^a Minimum χ^2 solution.

^b Lower bound on T and upper bound on $N(\text{HCN})$.

^c Optically thin solution with $R_e = R(\text{H}_2\text{O})$ from Table 2.

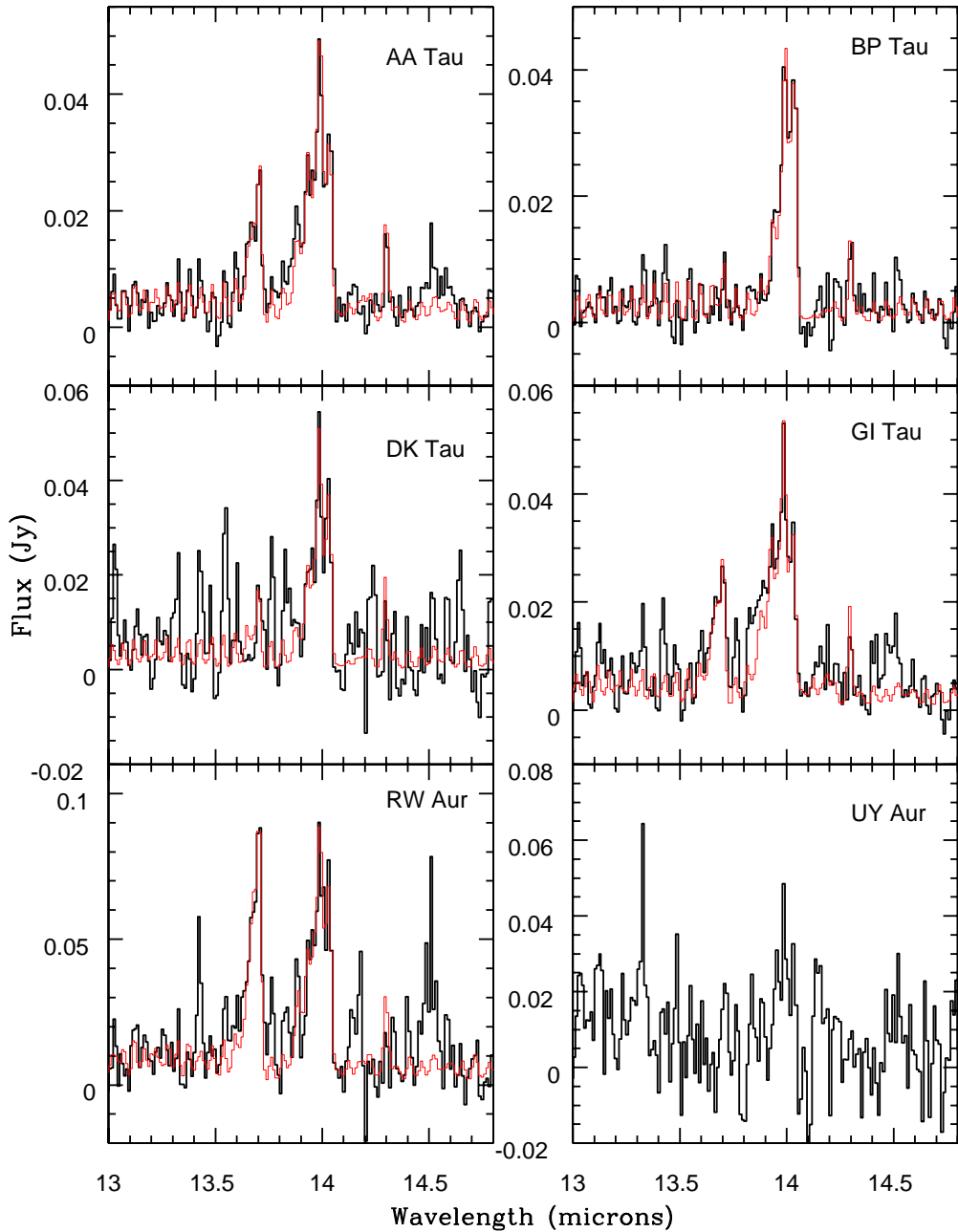


Figure 7. Synthetic spectra for HCN and C_2H_2 overplotted on the data. The data (thick black histogram) are the continuum-subtracted spectra with the best $\text{H}_2\text{O} + \text{OH}$ model subtracted. The model spectra (thin red histogram) are the best-fit parameters for HCN and C_2H_2 in Tables 3 and 4. The residual spectrum for UY Aur is plotted here to show the marginal detection of HCN, but a model spectrum was not calculated.

(A color version of this figure is available in the online journal.)

be placed on the HCN column by assuming that the emitting area for HCN is no larger than that for H_2O . This is a reasonable assumption given that the derived temperatures for HCN are similar to or greater than those found for H_2O . This limit, with $R_e(\text{HCN}) = R_e(\text{H}_2\text{O})$, is given as the “optically thin” solution in Table 3.

The best-fit HCN solution for AA Tau in Table 3 is very close to that reported in Carr & Najita (2008), although the uncertainty in column density and temperature is much larger in this paper. The reason for this difference is that the uncertainty given by Najita & Carr considered each parameter independently rather than looking at the two-dimensional confidence contours. This

also meant that the optically thin solution was not considered as a possibility in Carr & Najita.

As discussed in Section 4.1.2, the parameters for C_2H_2 are not determined independently, but the C_2H_2 column density relative to HCN is derived by assuming that C_2H_2 and HCN have the same temperature and emitting area. The ratio of the C_2H_2 -to-HCN column densities is given in Table 4 for the same three HCN solutions as in Table 3. The C_2H_2 column density ranges from 0.04 to 0.4 that of HCN for the best-fit HCN solution.

The assumption that C_2H_2 has the same excitation temperature as HCN produces a good fit to the C_2H_2 Q -branch in all three cases where the emission is well detected (see Figure 7),

Table 4
 $N(C_2H_2)/N(HCN)$ Ratio

Object	Best Fit	Optically Thick	Optically Thin
AA Tau	0.14	0.07	0.26
BP Tau	<0.035	<0.017	<0.051
DK Tau	0.04	0.006	0.10
GI Tau	0.25	0.14	0.29
RW Aur	0.38	0.19	0.43

Note. Ratio of C_2H_2 to HCN column density for the same cases as in Table 3.

but small temperature differences (~ 100 –200 K) cannot be ruled out. For RW Aur, we can independently fit the C_2H_2 band. This gave $T = 615$ K for C_2H_2 , compared to 690 K for HCN; the C_2H_2 column density is three times larger than that obtained assuming the same temperature and area. The χ^2 contour plots overlap significantly within their 90% confidence intervals. For the optically thin solution, the temperature is 715 K for C_2H_2 versus 745 K for HCN. Hence, the modeling uncertainties are consistent with the same temperature for HCN and C_2H_2 in RW Aur, though differences in temperature or emitting area would affect the derived relative column densities.

A sampling of best-fit models for the CO_2 emission is shown overplotted on the data in Figure 8. The observed spectra in Figure 8 show differences in the width of the CO_2 Q -branch, indicating a range in temperature and/or column density from object to object. However, the modeling is unable to place constraints on the CO_2 column density. The examples in Figure 6 show that the column density is not bounded within the 90% confidence contour in either the optically thin or the very optically thick limits. For this reason, we do not report column densities for CO_2 .

The models can place some constraint on the CO_2 excitation temperature. In Table 5, we give the CO_2 temperature at the minimum χ^2 solution and the allowable range for the temperature. At the lower temperature end, the 90% confidence contour often extends to temperatures below 75 K (e.g., Figure 6(b)), which is the minimum temperature at which the HITRAN partition functions can be applied. We also give the minimum radius for the emitting area that was found within the 90% confidence contour. This radius corresponds to a marginally optically thick solution at the high-temperature edge of the confidence area. The average of the best-fit temperatures in Table 5 is 340 K, but there is a considerable range between objects and in the allowable range for each object, and some stars (e.g., BP Tau) are very poorly constrained. The most noteworthy result is that the CO_2 temperature is usually lower, often substantially less, than the temperatures derived for H_2O and HCN.

4.2.2. H_2O and OH

The single temperature and column density LTE model provides a good first order match to the observed H_2O spectrum, though there are noticeable discrepancies. With the parameters for our best fits in the 12–16 μm region, the largest disagreements are seen for a number of strong, high-excitation lines ($E_u > 5000$ K) whose strengths are over-predicted by the model, particularly in the 16–18 μm region. Lower temperatures can provide a better fit to these lines, but at the expense of poor fits in the 12–16 μm interval. Meijerink et al. (2009) show in their non-LTE water calculations that transitions with higher energy levels and larger Einstein A -values will be the farthest from LTE. This strongly suggests that we are seeing the effect of

Table 5
Results for CO_2 Modeling

Object	T^a (K)	T_{range}^b (K)	R_{min}^c (AU)
AA Tau	325	120–490	0.8
BP Tau	425	75–800	0.1
DK Tau	220	75–300	2.0
GI Tau	100	75–360	0.9
RW Aur	510	140–680	0.6
UY Aur	200	75–390	1.5
AS353A	600	160–800	0.4

Notes.

^a Minimum χ^2 solution.

^b Temperature range within confidence interval.

^c Minimum emitting radius within confidence interval.

sub-thermal populations in many higher rotational levels. Our modeling also shows that the water spectra are dominated by rotational transitions in the ground vibrational state, with only minor contributions from transitions in the first vibrational state. The absence of excess emission from transitions in the first vibrational state, compared to the thermal LTE model, implies that infrared pumping in the fundamental rovibrational water bands is not significant.

The spectra in Figure 2 are remarkably similar in the relative strengths of H_2O features from star to star, suggesting similar excitation conditions and optical depth. This impression is confirmed by the best-fit models, which have a relatively narrow range in temperature and column density (Table 2). In fact, within the uncertainties, the results are consistent with a single temperature near 600 K. The H_2O column density shows some variation from star to star, but its range is less than a factor of five. For each of the objects modeled, the main H_2O lines are optically thick. The narrow parameter range for the H_2O lines is a more robust result than the absolute values for the parameters, because the actual values will be subject to systematic modeling effects, such as assumptions about LTE and local line broadening. Salyk et al. (2011) also find a small parameter range for H_2O , but with a somewhat different mean temperature.

Despite the similar temperature of the water emission among the sources in the sample, the emission fluxes vary by a factor of five (Table 6). Based on the modeling shown in Table 2, this is primarily the result of the *projected* emitting areas. The range of projected emitting radii is less than a factor of two, with a mean on the order of 1 AU. Thus, the water emission is likely arising from a similar range of disk radii.

The typical temperature required to match the rotational intensity distribution of the OH lines in the SH spectra was 4000 K. This result is similar to the high rotational temperature found from the OH spectrum of the transition disk TW Hya (Najita et al. 2010). For TW Hya, Najita et al. suggested the possibility of prompt OH emission from the photodissociation of H_2O . We will discuss this further in Section 6.3. A detailed analysis of the OH emission in this sample, which combines data from the SH and LH spectra, will be presented in a subsequent paper.

5. MOLECULAR FLUXES

5.1. Measurement of Fluxes

Fluxes for the molecular and atomic species observed in the SH spectrum were measured from the continuum-subtracted spectra. As described in Section 3, a spectral feature for a given species may contain unresolved contributions from

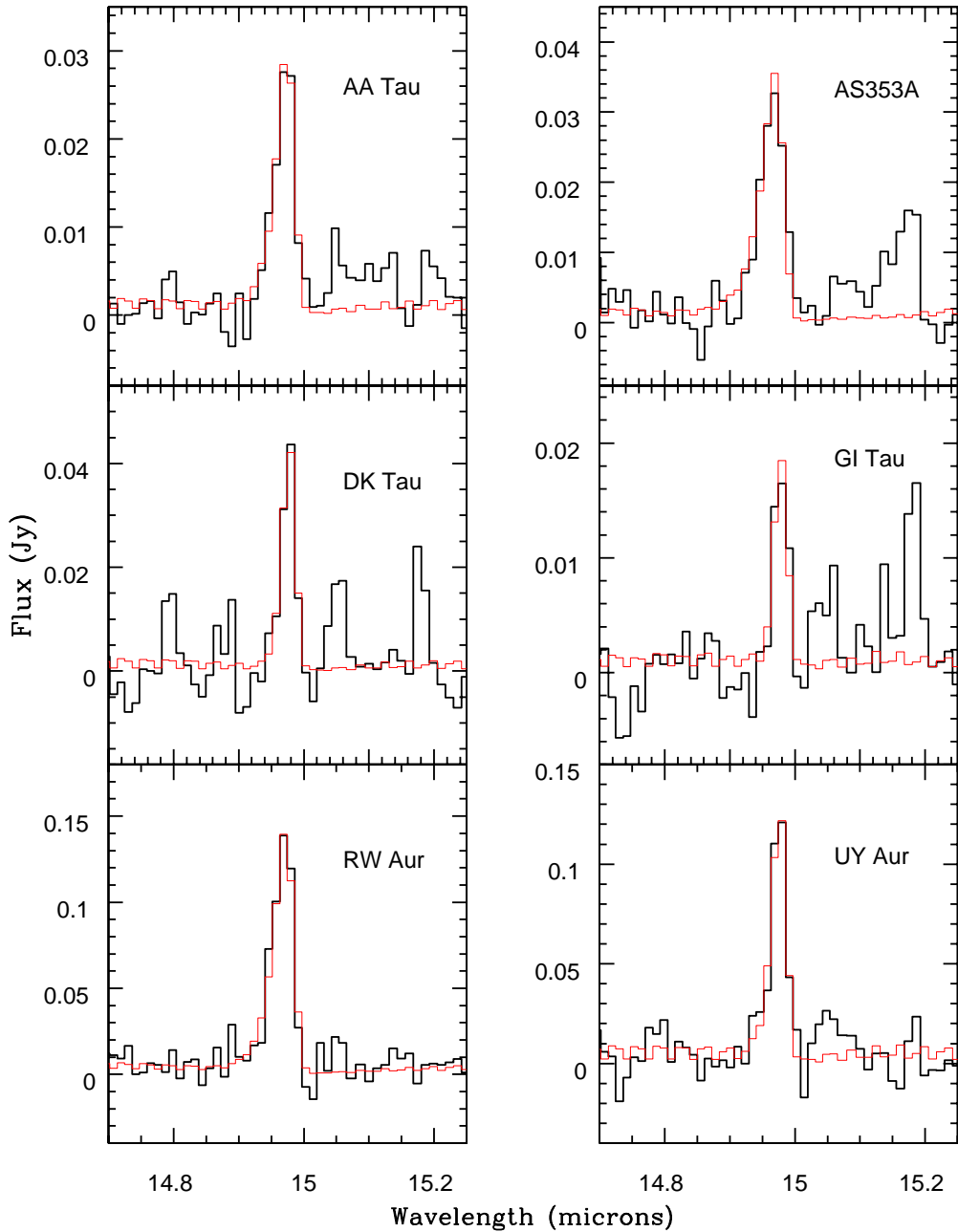


Figure 8. Synthetic spectra for CO₂ overplotted on the data. The data (thick black histogram) are the continuum-subtracted spectra with the best H₂O + OH + HCN + C₂H₂ model subtracted. The model spectra (thin red histogram) use the minimum χ^2 temperature solution in Table 5.

(A color version of this figure is available in the online journal.)

Table 6
Measured Molecular Fluxes

Object	H ₂ O	HCN	C ₂ H ₂	CO ₂	OH	H ₂ S(1)
AA Tau	4.8 (0.4)	6.6 (0.2)	1.5 (0.2)	1.3 (0.1)	0.6 (0.1)	0.30 (0.06)
BP Tau	6.6 (0.4)	5.4 (0.2)	<0.5	0.9 (0.1)	0.8 (0.1)	0.31 (0.09)
DG Tau	<2.6	<2.8	<1.9	<1.7	6.3 (0.7)	<0.70
DK Tau	15.4 (0.9)	5.9 (0.5)	0.5 (0.2)	1.4 (0.2)	2.0 (0.3)	<0.20
DO Tau	4.9 (0.8)	<1.4	<1.0	1.3 (0.4)	4.1 (0.4)	<0.38
GI Tau	6.0 (0.7)	7.0 (0.5)	2.2 (0.2)	0.7 (0.1)	1.0 (0.1)	0.59 (0.09)
GK Tau	4.6 (0.8)	<0.6	<0.5	0.4 (0.1)	1.3 (0.1)	0.35 (0.09)
RW Aur	21.7 (2.1)	9.6 (0.8)	6.7 (0.5)	6.8 (0.4)	2.8 (0.5)	1.31 (0.25)
UY Aur	12.1 (1.4)	<3.7 (2.0)	<0.7 (0.3)	4.5 (0.4)	3.1 (0.4)	<0.59
AS353A	<0.4	<0.5	<0.4	1.7 (0.1)	1.0 (0.1)	0.48 (0.09)
V1331Cyg	<1.0	<0.6	<0.5	0.5 (0.1)	0.9 (0.1)	<0.21

Note. Fluxes are 10^{-17} W m⁻². Upper limits are 2σ .

Table 7
Measured Atomic Fluxes

Object	[Ne II] ^a	H I ^b	[Fe II] ^c
AA Tau	1.25 (0.08)	0.20 (0.06)	...
BP Tau	0.28 (0.05)	0.90 (0.05)	...
DG Tau	25.7 (0.3)	7.4 (0.05)	6.4 (0.8)
DK Tau	0.73 (0.13)	1.4 (0.1)	...
DO Tau	0.91 (0.18)	2.7 (0.4)	...
GI Tau	0.73 (0.08)	1.0 (0.1)	...
GK Tau	0.53 (0.07)	1.1 (0.1)	...
RW Aur	0.5: (0.2)	5.3 (0.4)	...
UY Aur	2.41 (0.44)	1.5 (0.3)	...
AS353A	1.10 (0.11)	3.1 (0.1)	3.7 (0.2)
V1331 CYg	<0.2	2.2 (0.2)	8.3 (0.3)

Notes. Fluxes are $10^{-17} \text{ W m}^{-2}$. Upper limits are 2σ .

^a The $12.81 \mu\text{m}$ [Ne II] line.

^b The $12.37 \mu\text{m}$ H I line.

^c The $17.93 \mu\text{m}$ [Fe II] line is coincident with a H₂O feature and cannot be measured in objects with water emission.

other species, with the transitions of H₂O the most common contaminant. In order to account for this blending, we used the synthetic spectrum modeling described in Section 4. The fluxes for all species other than H₂O were measured after subtracting the best H₂O model from the spectrum. Synthetic spectra for additional species were subtracted as necessary, as described below. Measured fluxes for the molecular species are given in Table 6, and fluxes for the atomic lines are in Table 7. The uncertainties in the fluxes include both the pixel-to-pixel noise in the spectrum and an uncertainty on the continuum level.

The reported H₂O flux is the combined flux of the three H₂O features centered at 17.09 , 17.22 , and $17.34 \mu\text{m}$. Each of these spectral features is composed of multiple H₂O transitions. The three H₂O features are in close proximity to each other, well separated from other known molecular or atomic species, and among the strongest H₂O features in the SH spectral region. The H₂O flux was measured between 17.075 and $17.385 \mu\text{m}$. For OH, we measured the spectral feature at $14.64 \mu\text{m}$. This OH feature is the cleanest in the SH spectrum. It is dominated by a blend of the four components of the $N = 19$ transitions of the ground vibrational state of OH.

The Q -branches of HCN and C₂H₂ each contain some contribution from transitions of the other. Within this data set, this has a substantial effect only when C₂H₂ is weak or undetectable relative to HCN, which is the situation for BP Tau and DK Tau. The HCN flux was measured over the interval from 13.90 to $14.05 \mu\text{m}$, after subtracting the best-fit models for H₂O, OH, and C₂H₂. Similarly, the C₂H₂ flux was measured over the interval 13.65 – $13.735 \mu\text{m}$, after subtraction of the best-fit models for H₂O, OH, and HCN. The CO₂ Q -branch has a pair of prominent H₂O features that blend with the blue wing of the band. The CO₂ flux was measured from 14.93 to $14.997 \mu\text{m}$, with the blue edge of the interval chosen to minimize uncertainty from these H₂O features. A combined synthetic model for H₂O, OH, HCN, and C₂H₂ was subtracted before measuring the CO₂ flux.

The last molecular feature included in Table 6 is the $S(1)$ transition of molecular hydrogen at $17.03 \mu\text{m}$, which sits at a clean location between H₂O lines. The $S(2)$ rotational line at $12.28 \mu\text{m}$, on the other hand, is coincident with both H₂O and OH emission features (see Figure 3). These features normally dominate over any H₂ emission in our sample and make it impossible to measure the $S(2)$ line.

Fluxes for atomic lines are given in Table 7. Emission from the [Ne II] line at $12.81 \mu\text{m}$ is present in nearly every object, but it is often not prominent in the spectrum. Because weak features of H₂O, OH, HCN, and C₂H₂ are present near this line, we subtracted the combined synthetic molecular spectrum before measuring the [Ne II] flux. The strongest H I line in the spectrum is at $12.37 \mu\text{m}$. However, this line is blended with H₂O features that can contribute up to one-half the combined strength of the feature, based on the synthetic H₂O spectrum. This blending could add additional, but unknown, uncertainty to the H I strengths in Table 7. Line fluxes for the [Fe II] line at $17.93 \mu\text{m}$ are only given for the three stars that lack H₂O emission. For the rest of the objects, the strength of the $17.93 \mu\text{m}$ water feature predicted by the synthetic spectrum is equal to or greater than the observed strength, and hence it is not possible to extract any information on [Fe II] emission for these stars.

5.2. Absolute and Relative Fluxes

As noted in Section 3, the spectra in Figure 2 show a significant star-to-star variation in the relative fluxes of different molecular species. Figure 9 plots ratios of the measured molecular fluxes from Table 6 against one another. The first two panels show the ratios of HCN, C₂H₂, CO₂, and OH with respect to H₂O. The last panel compares the organic bands among themselves by plotting the ratio of C₂H₂ to HCN against CO₂ to HCN. These plots clearly establish that there is a real range in the relative fluxes of molecular species, about one order of magnitude in most cases. The range in the ratio CO₂/H₂O is somewhat smaller, a factor of four. The OH-to-H₂O flux ratio for all but one of the stars falls within a relatively narrow band, about a factor of two in width.

The absolute fluxes for each of the molecular species in Table 6 are also diverse, showing a range of about one order of magnitude for the Taurus sample. There is also an order of magnitude range seen in the line-to-continuum ratios (or equivalent widths) of the emission features.

6. DISCUSSION

6.1. Frequency and Origin of the Emission

While there is a substantial range in the fluxes, equivalent widths, and flux ratios of the detected molecular species in our sample, a common element is that mid-infrared molecular emission is ubiquitous. Emission in the high rotational lines of OH is present in all stars. Considering only the Taurus objects, the detection rates for H₂O and CO₂ are 89%. Such high detection rates are comparable to the frequency of CO fundamental in classical T Tauri stars (Najita et al. 2003; Salyk et al. 2011). Emission in the Q -branches of HCN and C₂H₂ is less common, at 67% and 44%. These molecular detection rates are comparable to those found in larger samples of classical T Tauri stars (Pontoppidan et al. 2010b).

As we initially reported for the star AA Tau, the analysis of the mid-infrared molecular emission in this larger sample of classical T Tauri stars yields emitting areas and temperatures that are consistent with an origin in the inner few AU of the circumstellar disk. We find that the molecule with the best constrained parameters, H₂O, has projected emitting radii of $\sim 1 \text{ AU}$, implying deprojected radii $< 2 \text{ AU}$. The best-fit values for HCN give smaller emitting areas, 0.1–0.4 that of H₂O, and projected radii of 0.4–0.6 AU. However, equal areas for HCN and H₂O are also consistent with the errors (Section 4.2.1). The temperatures for H₂O, HCN, and C₂H₂ are constrained to be

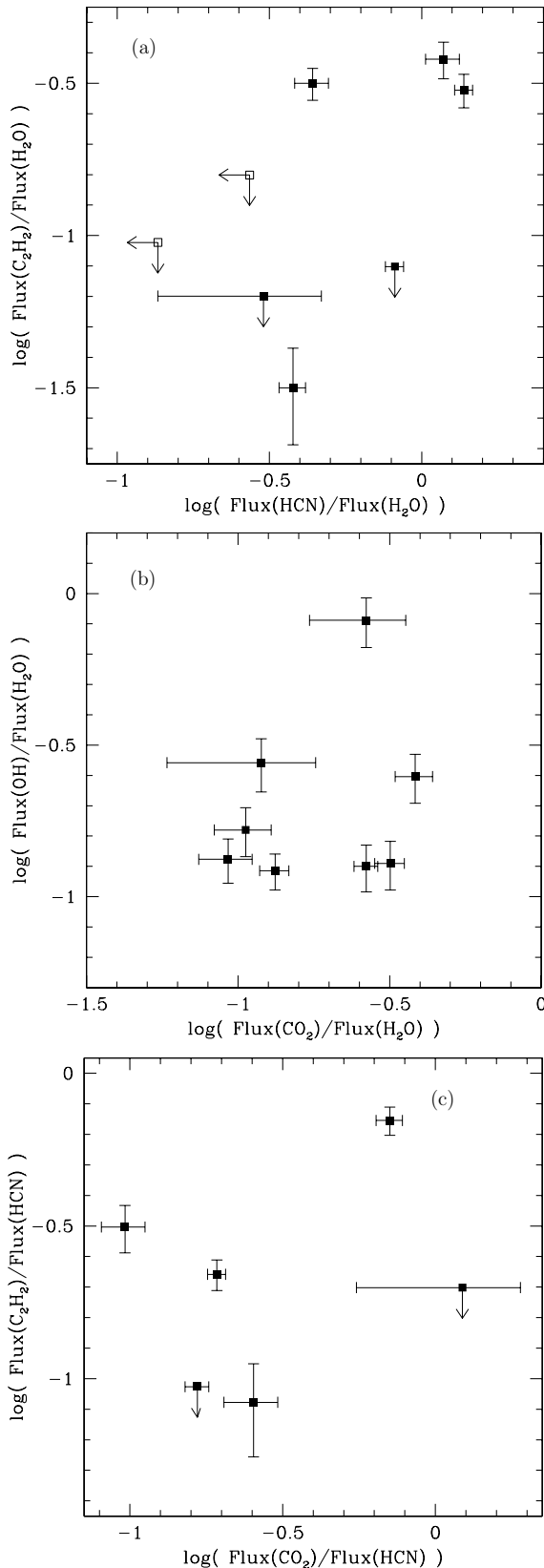


Figure 9. log-log plots of different flux ratios against one another for measured molecules. All limits (arrows) are 2σ . (a) Flux ratio of $\text{C}_2\text{H}_2/\text{H}_2\text{O}$ vs. $\text{HCN}/\text{H}_2\text{O}$. (b) Flux ratio of $\text{OH}/\text{H}_2\text{O}$ vs. $\text{CO}_2/\text{H}_2\text{O}$. (c) Flux ratio of $\text{C}_2\text{H}_2/\text{HCN}$ vs. CO_2/HCN .

in the range of 400–800 K. The temperature for CO_2 , while often more uncertain, is generally lower and in the range of

100–600 K. These temperatures are consistent with models that calculate the vertical thermal structure of the molecular gas at radii within a couple of AU of the star (Glassgold et al. 2004, 2009; Nomura et al. 2007; Woitke et al. 2009).

The interpretation of a disk origin for the molecular emission is corroborated by the velocity profiles of H_2O lines that have been measured for a small number of objects with high-resolution mid-infrared spectroscopy (Pontoppidan et al. 2010a; Knez et al. 2007). The line widths are consistent with disk radii of ~ 1 AU and similar to those measured for the CO fundamental transitions. The high critical densities required for thermal excitation of the mid-infrared water transitions (up to 10^{12} cm^{-3} ; Meijerink et al. 2009) provide additional support that the lines form in a disk atmosphere.

Shocks associated with unresolved outflows within the IRS slit are not likely to explain the molecular emission, because the mid-infrared spectra for the T Tauri stars are dissimilar from those observed for outflows. The *Spitzer* IRS spectra of protostellar outflows are generally dominated by emission in the rotational transitions of H_2 and the atomic fine structure [S I] $25 \mu\text{m}$, [Fe II] $26 \mu\text{m}$, and [Si II] $35 \mu\text{m}$ lines (e.g., Neufeld et al. 2009; Dionatos et al. 2010). When hot water has been detected (Melnick et al. 2008), relatively few H_2O transitions are seen, all in the LH module at $\lambda > 29 \mu\text{m}$. This water emission indicates low gas densities $\sim 10^5 \text{ cm}^{-3}$ and is consistent with non-dissociative shocks, in agreement with conclusions reached for water emission observed from outflows in the far-infrared (e.g., Giannini et al. 2001; Benedettini et al. 2002; Nisini et al. 2010). A potential exception to the above is the possibility of a shock contribution to the OH emission seen in the T Tauri stars, given that similarly high rotational transitions of OH have been detected in one Herbig-Haro object (Tappe et al. 2008; see Section 6.3). Dissociative shocks could explain some of the atomic lines observed in our sample. Emission from [Fe II] $26 \mu\text{m}$, and sometimes [Si II] $35 \mu\text{m}$, is present in stars with strong jets; the [Fe II] $17.9 \mu\text{m}$ transition is also strong in some of these stars, though this line is not apparent in outflows. In addition, the exceptionally strong [Ne II] emission from DG Tau shows a blueshift of 130 km s^{-1} in our data and is likely to originate from a jet (see Guedel et al. 2010 on jet contributions to [Ne II] emission).

6.2. Water Emission

We find that the properties of the water emission are fairly similar among the sources in our sample, with a narrow range in the LTE temperature (with a mean of ~ 600 K) and H_2O column densities $\sim 10^{18} \text{ cm}^{-2}$ (see also Salyk et al. 2011). The uniformity in the water emission spectra (optically thick emission with similar excitation temperature) is remarkable. Given possible variations in the grain properties, UV and X-ray irradiation, accretion heating, and transport processes of disk atmospheres, one might imagine that inner disk atmospheres and the water emission from them might be highly diverse. This does not appear to be the case.

The narrow temperature range suggests that H_2O could play a role in regulating the temperature of the gaseous disk atmosphere. The large H_2O line luminosities determined from the mid-infrared H_2O spectra of disks demonstrate that water is a major gas coolant of the disk atmosphere (Pontoppidan et al. 2010b). At the same time, water can contribute to the gas heating through absorption of FUV radiation from the accretion shocks and near-infrared flux from the star. If absorption in the FUV bands of water dominates the gas heating, then water self-

shielding will place an upper limit on the total column of warm H_2O , at $\sim 10^{18} \text{ cm}^{-2}$ (Bethell & Bergin 2009), a value that is similar to our derived water column densities.

The thermal-chemical disk atmosphere models of Glassgold et al. (2009) reproduce well the water temperatures and column densities that we derive. Particularly interesting is their finding that the molecular emitting layer has a temperature structure that does not change much over a range in disk radii (0.25–2 AU), while maintaining water column densities of 10^{17} – 10^{18} cm^{-2} . Water heating and cooling were not included in their models; it would be interesting to add these processes to determine their effect on the temperature structure of the disk atmosphere.

6.3. OH Emission

Our detection of high-rotational OH transitions suggests the role of UV irradiation in producing the OH emission. The $14.65 \mu\text{m}$ feature, along with the other OH features in the SH spectrum, has upper energy levels several 1000 K above ground and relative intensities indicating a characteristic rotational temperature of ~ 4000 K (Section 4.2.2). Hot OH emission of this kind is prominent in the SH spectrum of the transition object TW Hya and has been suggested to result from the photodissociation of water by stellar UV (Najita et al. 2010). Photodissociation by FUV photons in the second absorption band of water ($\lambda = 1200$ – 1400 \AA) produces OH molecules in highly excited rotational levels but predominantly in the ground vibrational state (Harich et al. 2000).

The hot OH emission we measure in the SH module differs from the warm (≤ 1000 K) OH emission detected via lower rotational OH lines in the LH module (Carr & Najita 2008; Salyk et al. 2011). The presence of both hot and warm OH components can be understood if the OH molecules produced by photodissociation first emit hot (prompt) OH emission and then thermally relax to the temperature of the surrounding gas, producing cooler thermal emission (Najita et al. 2010).

Glassgold et al. (2009) suggested the possible role of UV irradiation in dissociating disk water vapor to produce abundant OH, noting that the OH column densities predicted by their thermal-chemical models fell far short of those reported for the warm (~ 500 K) OH emission for AA Tau (Carr & Najita 2008). Bethell & Bergin (2009) have shown that the column densities of the warm OH emission agree well with the predictions of a simple UV-irradiated slab model in which OH is produced by the photodissociation of water in the disk surface layers. In their model, the maximum OH column is limited by the FUV opacity due to OH and H_2O self-shielding.

Consistent with a role for UV radiation, we find that the $14.65 \mu\text{m}$ OH flux increases with stellar accretion rate (Figure 10), which is a measure of the UV flux of the system. We also found that the flux ratio of the $14.65 \mu\text{m}$ OH feature (non-thermal) and the $17 \mu\text{m}$ water feature (thermal) is relatively constant among a majority of sources in our sample (Figure 9), suggesting a close connection. One possibility is that they are both driven by stellar accretion, with the OH produced by UV dissociation and the water heated by UV radiation and/or accretion heating in the disk. We note that the highest accretion rate objects in our sample show OH emission but not H_2O emission. This suggests that at sufficiently high FUV fluxes, H_2O may be destroyed in favor of OH in the warm disk atmosphere (Bethell & Bergin 2009). Extending such an effect to the higher FUV fluxes for Herbig Ae/Be stars may explain the detection of OH but not H_2O emission from Herbig Ae/Be stars (Mandell et al. 2008; Pontoppidan et al. 2010b).

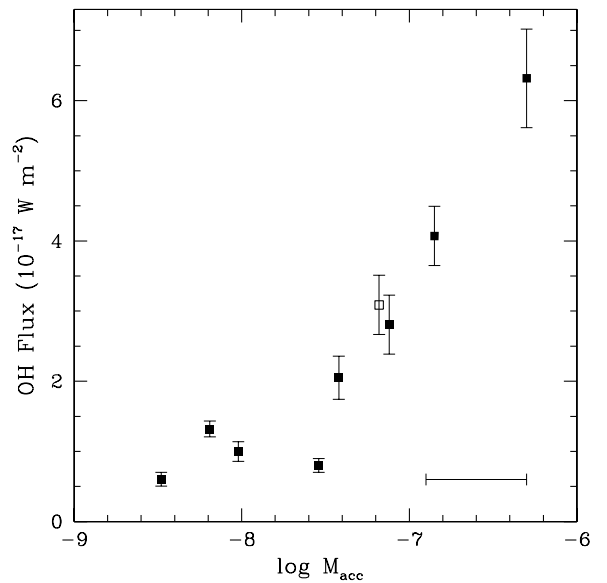


Figure 10. OH emission flux vs. \log of accretion rate. The accretion rate is in $M_{\odot} \text{ yr}^{-1}$. The open square is for the binary UY Aur. The error bar in the lower right suggests a possible range in variability in the accretion rate.

An alternative interpretation is that some fraction of the OH detected from the higher accretion rate objects in our sample may arise in shocks close to the star that are produced by the outflows in these systems (DG Tau, AS353A, V1331 Cyg). Tappe et al. (2008) detected highly excited OH emission in the *Spitzer* spectrum of young stellar outflow HH 211. That emission is comparable, but with higher rotational levels, to that observed here. They attributed the origin of the OH emission to H_2O that is the photodesorbed from grains and then photodissociated by the UV radiation generated in the terminal outflow shock.

6.4. Organic Emission

The observed variation in the strength of the organic emission features (HCN, C_2H_2 , CO_2) is difficult to interpret. The relative fluxes of the organic features and their strengths with respect to H_2O vary, often by an order of magnitude or more (Figure 9). The ratio of the derived column density of C_2H_2 to HCN shows a similar range (Table 4). A number of factors could potentially impact the chemistry or structure of the disk atmosphere and produce variations in the relative molecular fluxes. Some obvious physical processes include UV and X-ray irradiation of the disk, accretion heating, and grain settling. We examined the position of points in Figure 9 with respect to measured system parameters that track these processes to search for any patterns (e.g., whether all stars with strong C_2H_2 relative to H_2O have high X-ray fluxes). We considered the mass accretion rate (Table 1) as a measure of UV radiation and accretion heating, the un-absorbed X-ray flux (Guedel et al. 2010), and the mid-infrared spectral index n_{13-25} as a measure of grain settling (Furlan et al. 2006).

We did not find any obvious patterns that predict the behavior of the relative fluxes of the organic molecules with respect to these parameters. Perhaps larger data sets are required to reveal the influence of a particular parameter, particularly if multiple parameters play a role. Alternatively, the lack of an obvious predictor could indicate the importance of another parameter that has not been explored.

One possible factor, which lacks a direct observable, is variations in the C/O ratio of the gas. Such variations are

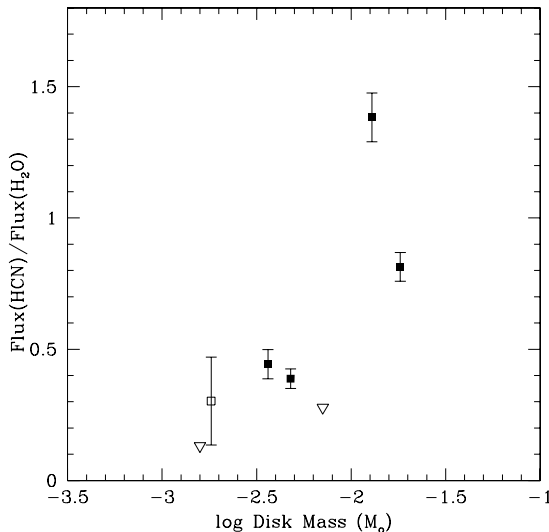


Figure 11. Flux ratio of HCN to H₂O plotted against disk mass. Inverted triangles are upper limits (2 σ) and correspond to stars with non-detections of HCN emission. The open square is for the binary UY Aur, which also has a marginal detection for HCN.

expected to arise in the inner disk as a consequence of the growth and transport of icy material over sizes ranging from grains to planetesimals and protoplanets. As described by Ciesla & Cuzzi (2006, and references therein), when icy grains in the outer disk grow into approximately meter-sized bodies, they experience torques that lead them to migrate inward more rapidly than the surrounding gas. As they pass the “snow line” on their inward journey, they vaporize, pumping water (and oxygen nuclei) into the gas phase. If these bodies instead collide and grow to planetesimal size while they are still beyond the snow line, they drop out of the accretion flow and can thereby sequester water (and oxygen) in the outer disk.

In the former case, the hydration of the gaseous inner disk leads to a reduction in the C/O ratio. In the latter case, the sequestration of water in the outer disk leads to an enhancement in the C/O ratio. The detailed models of Ciesla & Cuzzi (2006) illustrate how the water abundance in the inner disk (and hence the C/O ratio) can be enhanced or reduced by an order of magnitude relative to its initial value, depending on the efficiency with which large bodies grow. Higher C/O ratios would tend to enhance the formation of organic molecules.

As the efficiency with which large bodies form may depend on the initial conditions (e.g., disk mass), we could expect a range in the C/O ratios of the inner disks among T Tauri stars of similar age, such as in our sample. Higher mass disks, which may have experienced more extensive planetesimal and protoplanet formation, might be expected to have a higher C/O ratio and enhanced abundances of organic molecules in the inner disk. Interestingly, the two sources in our sample with the largest HCN/H₂O flux ratios (AA Tau and BP Tau) are the two sources with the largest disk masses (Figure 11 plots HCN/H₂O versus disk mass, using the disk masses in Table 1). Studies of larger samples are needed to explore the reality and implications of a relationship between HCN/H₂O and disk mass.

7. ABUNDANCES

7.1. Inner Disk Abundances

Disk molecular abundances can provide valuable insights into disk chemical and physical processes. However, extracting

abundances from the infrared molecular spectra is far from trivial. A simple approach is to compare the relative column densities of molecules derived from the LTE modeling, although this approach does have issues with regard to both interpretation and accuracy.

First, the molecules measured in the *Spitzer* IRS spectra only provide a global average of the disk emission, and it is not known to what extent different molecules occupy the same volume, given the absence of spatial information. The LTE modeling implies comparable temperatures for H₂O, HCN, and C₂H₂, suggesting that they are similar in their distributions, but the CO₂ emission may arise from regions of cooler gas. Eventually, line profiles obtained with high-resolution spectrographs can provide information on the relative radial distribution of the emission by using velocity and assumed Keplerian motion as a proxy for radius. However, various molecular species, even those arising from the same disk radii, could still have different vertical distributions in the atmosphere. Thermal-chemical models of disk atmospheres may provide insights into whether certain molecular species are likely to be cospatial. The value of such insights depends critically on vetting the models by comparing their predicted structures with observations of disks. The data presented here provide a small step in that direction.

Second, it is worth noting that the infrared molecular emission is likely to probe only the atmosphere of the disk. The inner disks of classical T Tauri stars are optically thick at mid-infrared wavelengths, and the observed emission lines probably arise in a temperature inversion above the disk photosphere. A key question then is whether the composition in the line formation region is representative of the vertically integrated column of the disk. The chemistry in the upper disk atmosphere is likely to be different than that in deeper layers toward the mid-plane. Irradiation by UV and X-rays, in particular, is expected to be important; in addition, the densities are lower, and gas-to-dust ratios will be higher than in the mid-plane, if grain settling has occurred. Vertical chemical gradients could, however, be smoothed or reduced by mixing, if the timescale for vertical transport is short with respect to the key chemical timescales.

In contrast to the likely true physical situation, the model used to determine the column density and temperature from the spectra assumes a plane parallel layer for each molecule that is homogeneous in both vertical and radial directions and that the rotational and vibrational level populations are described by a single Boltzmann distribution. In spite of its simplicity, the LTE model does a surprisingly reasonable job of fitting the observed spectra. There are differences between the calculated and observed H₂O spectra, which suggest that some higher energy levels are sub-thermally populated (Section 4.2.2). This is not surprising given the real possibility that gas densities in the upper atmosphere could be too low to thermalize all the level populations. Radiative pumping may also contribute to the excitation, though there is no clear evidence that this is occurring (Section 4.2). Finally, it should be noted that the adopted fitting procedures and other modeling assumptions can also have considerable impact on the results (cf. Salyk et al. 2011).

With these known caveats, we examine the relative column densities of H₂O, HCN, and C₂H₂ for the T Tauri stars in our sample. In Figure 12, is plotted the column density ratio of C₂H₂ to HCN versus the ratio of HCN to H₂O for the five stars where we could model the HCN emission. The large error bars on the HCN/H₂O ratio reflect the large parameter range allowed by the fits on the HCN column density. The lower end on the

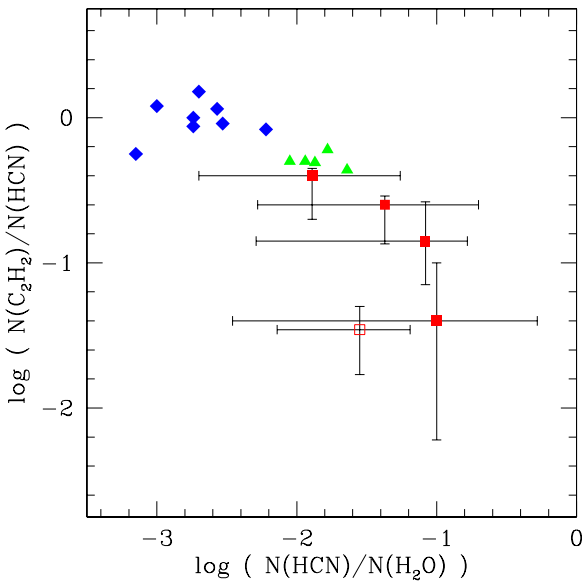


Figure 12. Line-of-sight column density of C_2H_2 to HCN plotted against the column density of HCN to H_2O . The squares are the column density ratios for T Tauri star disks from the LTE slab models in this paper. BP Tau, plotted as an open square, has an upper limit on the $\text{C}_2\text{H}_2/\text{HCN}$ ratio. The lower error bar on $\text{HCN}/\text{H}_2\text{O}$ for each star corresponds to the optically thin solution with equal emitting areas for HCN and H_2O . The triangles are column density ratios for hot molecular cores around massive protostars derived from mid-infrared absorption measurements. The diamonds are ratios of the abundances in comets as determined from near-infrared spectroscopy. Data for hot cores and comets are from references given in the text.

(A color version of this figure is available in the online journal.)

error bars corresponds to the optically thin solution with the assumption of equal HCN and H_2O emitting areas. The best-fit points for the HCN column are a few percent that of H_2O , with an average ratio of 0.04. If we treat the upper and lower error bars as the range of possible systematic effects in fitting the HCN band, then the likely range for $\text{HCN}/\text{H}_2\text{O}$ is 0.005–0.15. The smaller error bars for the $\text{C}_2\text{H}_2/\text{HCN}$ column density ratio result from the assumption that C_2H_2 and HCN have the same temperature and emitting areas. Under these assumptions, there is a real range in the C_2H_2 -to-HCN ratio, from 0.04 to 0.4, with an average of ~ 0.1 .

7.2. Comparison to Envelopes, Outer Disks, Comets, and Hot Cores

We can compare the inner disk abundances described above with the abundances of gaseous protostellar envelopes, outer T Tauri disks, and comets. Since these systems probe the gas- and solid-phase abundances at larger radii than the inner disk, they represent chemical precursors that the inner disk ultimately inherits as a consequence of envelope infall, disk accretion, and solid-body migration. Such a comparison may lead to insights into the extent of chemical processing in disks.

The HCN/CO abundance ratios for inner disks appear to be a few orders of magnitude larger than the values for low-mass protostellar envelopes and the outer disks of T Tauri stars. Prestellar cores, Class 0 sources, and Class 1 sources, which are the evolutionary precursors of T Tauri stars, typically have HCN/CO mass ratios of 10^{-4} or smaller in the gas phase, as measured in millimeter emission lines (Jørgensen et al. 2004). The outer disks surrounding T Tauri stars are also found to have HCN/CO column density ratios of a few times 10^{-4} or smaller (Thi et al. 2004; Dutrey et al. 1997). In comparison,

our inferred HCN abundance relative to H_2O for inner disks is approximately a few percent. If we assume that the disks in our sample have $\text{CO}/\text{H}_2\text{O}$ column density ratios ~ 1 , as found for AA Tau and other T Tauri stars (Carr & Najita 2008; Salyk et al. 2011), then the HCN/CO ratios for inner disks are also a few percent. Similarly high HCN/CO ratios are derived from infrared absorption measurements toward two low-mass young stars where the absorption is interpreted as arising in the inner region of a disk seen close to edge-on: HCN/CO is 0.025 in IRS 46 (Lahuis et al. 2006a) and 0.014 in GV Tau N (Gibb et al. 2007, 2008). Some of the difference between the gas-phase HCN/CO ratio of inner disks and those of envelopes and outer disks may be accounted for by freeze-out onto grains, which is thought to be substantial (e.g., Jørgensen et al. 2004).

Cometary abundances provide insight into what was frozen out onto grains, because comets are made of icy material that was originally present in the Jupiter–Saturn region and in the outer solar nebula (the Kuiper Belt) during the formation of the solar system. Analyses of near-infrared spectroscopy of comets find a mean $\text{HCN}/\text{H}_2\text{O}$ abundance ratio of 0.0026 and a mean $\text{C}_2\text{H}_2/\text{H}_2\text{O}$ abundance ratio of 0.0024; thus the $\text{C}_2\text{H}_2/\text{HCN}$ ratio is typically ~ 1 (DiSanti et al. 2009; DiSanti & Mumma 2008). In comparison, the $\text{HCN}/\text{H}_2\text{O}$ ratios we find for inner disks are all systematically higher than those found for comets, by approximately an order of magnitude on average (see Figure 12). The $\text{C}_2\text{H}_2/\text{HCN}$ abundance ratios for inner disks are also systematically lower than those of comets by a factor of 2–20, or approximately an order of magnitude on average.

A larger $\text{HCN}/\text{H}_2\text{O}$ ratio for gaseous inner disks, compared to both comets and gaseous outer disks, would suggest that the abundances of inner disks are not simply the result of gas and icy material migrating from the outer to the inner disk. Instead, further gas-phase processing may occur within the snow line following the evaporation of icy material.

Our results can also be compared to the abundances of hot cores, the molecular envelopes surrounding high-mass protostars. Hot cores have long been known to show a rich chemistry with complex organic molecules. The same molecules we observe in emission in the T Tauri stars have also been detected in absorption in mid-infrared bands toward several hot cores using *Infrared Space Observatory* (ISO; Lahuis & van Dishoeck 2000; Boonman & van Dishoeck 2003). The derived gas temperatures for the absorbing gas are in the same range as we found for the T Tauri stars. The ratios of reported absorption columns are plotted in Figure 12. Typical values are $\text{HCN}/\text{H}_2\text{O} \sim 0.01$, larger than those of comets and within the range found here for inner disks, and $\text{C}_2\text{H}_2/\text{HCN} \sim 0.5$ (at the upper end of the range inferred here for inner disks).

Thus the *average* inner disk atmosphere appears to have similar or slightly higher HCN abundance with respect to H_2O than do hot cores. However, the HCN abundance would be at least an order of magnitude larger if CO were taken as the reference molecule. This is because the infrared absorption columns toward hot cores have an average $\text{CO}/\text{H}_2\text{O}$ column density ratio of 10, whereas the disks in our sample are more likely to have $\text{CO}/\text{H}_2\text{O}$ column density ratios ~ 1 , (Carr & Najita 2008; Salyk et al. 2011).

Similar chemical processes could be in operation in hot cores and inner disks. In hot cores, the warm gas phase follows the sublimation of molecules from icy grain mantles, where the rich chemistry that is observed is the result of some combination of grain-surface and warm gas-phase reactions. Inner disks present

an analogous situation, in that the warm gas-phase molecules we observe represent material that was desorbed from grains as it migrated inward from the outer disk. Because of these similarities, hot core chemistry may serve as a rough guide to the kind of chemical synthesis that may be occurring in inner disks. Numerous complex molecules are detected in hot cores (e.g., Herbst & van Dishoeck 2009). Similar complex species could be present in inner disks.

7.3. Comparison to Chemical Models of Inner Disks

Several features of the molecular emission we observe are reproduced in recent chemical models of inner disks. The thermal-chemical calculation of Glassgold et al. (2009) is able to account for the large column densities ($\sim 10^{18} \text{ cm}^{-2}$) and warm temperatures ($\sim 500 \text{ K}$) of the water emission by invoking H₂ formation on warm grains and (accretion-related) mechanical heating in the disk atmosphere. Grain settling also plays a role in achieving large column densities of warm molecular gas, by reducing the gas-grain cooling in the atmosphere (Glassgold et al. 2004, 2009).

In the thermal-chemical protoplanetary disk model of Woitke et al. (2009; PRODIMO), water is also present in the inner disk atmosphere although at much lower column densities ($< 10^{14} \text{ cm}^{-2}$ above 200 K at 1 AU) than we measure. Willacy & Woods (2009) also calculate the gas temperature in their model of disk atmospheres. They find very large columns of warm ($> 1000 \text{ K}$) H₂O ($\sim 10^{19} \text{ cm}^{-2}$) at 1 AU, much larger than those measured here. The different dominant sources of heating and assumptions regarding grain abundances in these models may be partly responsible for the very different predictions.

The disk chemistry calculation of Agúndez et al. (2008) considers the formation of organic molecules as well as water. In lieu of a thermal calculation, they adopt an existing model for the temperature and density structure of the disk (D'Alessio et al. 1998, 1999), which is then irradiated by a (primarily) interstellar FUV field. At 1 AU, the resulting HCN vertical column density at the disk surface is $\sim 2 \times 10^{16} \text{ cm}^{-2}$, with a C₂H₂ column density that is ~ 10 times smaller and H₂O and CO columns $\sim 2 \times 10^{17} \text{ cm}^{-2}$ and $\sim 8 \times 10^{17} \text{ cm}^{-2}$. These values are similar to the values we measure for inner disk atmospheres. At 2 AU, the HCN vertical column density at the disk surface is much smaller, $\sim 5 \times 10^{13} \text{ cm}^{-2}$, with a C₂H₂ column density that is ~ 5 times smaller. If these results are a guide to what to expect in disk atmospheres, the declining HCN and C₂H₂ abundances beyond 1 AU suggest that HCN and C₂H₂ emission would be limited to the inner 1–2 AU of the disk, consistent with our results.

An important difference between the observations and the Agúndez et al. (2008) disk atmosphere model is the gas temperature. Because the gas temperature in the calculation is taken to equal the dust temperature, the surface molecular layers are much cooler ($\leq 300 \text{ K}$) than are observed (~ 500 –700 K). Warmer disk atmospheres would tend to further enhance the molecular abundances (Figure 1 of Agúndez et al. 2008).

Willacy & Woods (2009) also study HCN and C₂H₂. At 1 AU, they find vertical columns of warm HCN ($\sim 4 \times 10^{16} \text{ cm}^{-2}$) that are comparable to those measured here, accompanied by much smaller columns of C₂H₂ ($\sim 9 \times 10^8 \text{ cm}^{-2}$) than we measure. Both species are present at warmer temperatures ($> 1000 \text{ K}$) than we measure. The differences between these models and the observations may help to guide the future development of disk atmosphere models.

8. SUMMARY

One notable discovery of the *Spitzer* mission is that molecular emission is common in the mid-infrared spectra of T Tauri stars. In the sample of 11 classical T Tauri stars studied in this report, we find high detection rates of H₂O and OH rotational lines and rovibrational bands of CO₂, HCN, and C₂H₂. *Spitzer* spectroscopy of larger samples of T Tauri stars (Pontoppidan et al. 2010b) produces similar results. Our sample shows significant star-to-star variation (up to an order of magnitude) in the absolute molecular fluxes, the equivalent widths, and the relative flux ratios of different molecules.

We estimated gas temperatures, column densities, and emitting areas using an LTE slab model. For H₂O, we find a similar temperature for each object, about 600 K, a narrow range for LOS column density, $\sim 10^{18} \text{ cm}^{-2}$, and projected emitting areas of radius $\sim 1 \text{ AU}$. Comparable or potentially higher temperatures are derived for HCN, in the range of 500–800 K. The C₂H₂ *Q*-branch is consistent with having the same temperature as HCN. The best fits to the HCN spectra require a smaller emitting area for HCN than for H₂O, though similar emitting areas are not ruled out. Fits to the CO₂ *Q*-branch are more uncertain, but imply lower temperatures than the other molecules (100–600 K), with an average best-fit temperature of 350 K. This suggests that the CO₂ emission arises in a cooler volume in the disk, either at larger radii or at a different vertical height.

The gas temperatures, emitting areas, and high critical densities for the observed H₂O transitions are consistent with gas in a disk atmosphere at radii within 2 AU of the star. Hence, the observed mid-infrared molecular emission traces gas in the inner planet formation region, radii that correspond to the terrestrial planet region in the solar system and that fall within the generally accepted location of the snow line in protoplanetary disks.

We discuss how the HCN/H₂O or HCN/CO column density ratios are roughly a few percent, which is about an order of magnitude larger than the average ratio derived for comets and at least two orders of magnitude larger than those measured for the outer disks of T Tauri stars and low-mass protostellar cores. The HCN/H₂O ratio for inner disks is comparable to the ratios derived for hot molecular cores around massive protostars, but the HCN/CO ratios could be an order of magnitude larger. These comparisons suggest a picture where the gas-phase abundances in the inner disk are the result of chemically active disks, rather than simple infall of material from the protostellar envelope and inward migration through the outer disk.

The H₂O emission spectra are remarkably similar from star to star, which is reflected in the narrow range of model parameters and implies limited variation in H₂O excitation conditions and optical depth. High rotational transitions of OH are present in all spectra and are likely due to prompt emission of OH following FUV photodissociation of water. The role of UV radiation and a connection between OH and H₂O are supported by the increase in OH emission flux with increasing stellar accretion rate and the relatively small scatter in the OH/H₂O flux ratio. We propose that some of the wide variation in the relative emission strengths of the organic molecules with respect to H₂O could be related to star-to-star differences in the C/O ratio (the oxygen fugacity) of the inner disk gas that affects the organic chemistry. Differing C/O ratios could result from enhancements or depletions of water in the inner disk depending on the efficiency of the growth of large bodies beyond the snow line (Ciesla & Cuzzi 2006). The objects in our sample with the largest HCN/H₂O flux ratios also have the largest disk masses. We speculate that

this can be understood if higher mass disks are more efficient at forming planetesimals and sequestering water in the outer disk, leading to higher C/O ratios and enhanced abundances of organic molecules in the inner disk.

This work is based on observations made with the *Spitzer Space Telescope*, which is operated by the Jet Propulsion Laboratory, California Institute of Technology under a contract with NASA. Support for this work was provided by NASA. Basic research in infrared astrophysics at the Naval Research Laboratory is supported by 6.1 base funding.

REFERENCES

Agúndez, M., Cernicharo, J., & Goicoechea, J. R. 2008, *A&A*, **483**, 831

Andrews, S. M., & Williams, J. P. 2005, *ApJ*, **631**, 1134

Barber, R. J., Tennyson, J., Harris, G. J., & Tolchenov, R. N. 2006, *MNRAS*, **368**, 1087

Benedettini, M., Viti, S., Giannini, T., Nisini, B., Goldsmith, P. F., & Saraceno, P. 2002, *A&A*, **395**, 657

Bethell, T., & Bergin, E. 2009, *Science*, **326**, 1675

Biscaya, A. M., Rieke, G. H., Narayanan, G., Luhman, K. L., & Young, E. T. 1997, *ApJ*, **491**, 359

Boonman, A. M. S., & van Dishoeck, E. F. 2003, *A&A*, **403**, 1003

Carr, J. S. 1989, *ApJ*, **345**, 522

Carr, J. S., & Najita, J. R. 2008, *Science*, **319**, 1504

Chihara, H., Koike, C., Tsuchiya, A., Tachibana, S., & Sakamoto, D. 2002, *A&A*, **391**, 267

Ciesla, F. J., & Cuzzi, J. N. 2006, *Icarus*, **181**, 178

D'Alessio, P., Calvet, N., Hartmann, L., Lizano, S., & Canto, J. 1999, *ApJ*, **527**, 893

D'Alessio, P., Canto, J., Hartmann, L., Calvet, N., & Lizano, S. 1998, *ApJ*, **500**, 411

Dionatos, O., Nisini, B., Cabrit, S., Kristensen, L., & Pineau Des Forets, G. 2010, *A&A*, **521**, 7

DiSanti, M. A., & Mumma, M. J. 2008, *Space Sci. Rev.*, **138**, 127

DiSanti, M. A., Villanueva, G. L., Milam, S. N., Zack, L. N., Bonev, B. P., Mumma, M. J., Ziurys, L. M., & Anderson, W. M. 2009, *Icarus*, **203**, 589

Doppmann, G. W., Najita, J. R., & Carr, J. S. 2008, *ApJ*, **685**, 298

Doppmann, G. W., Najita, J. R., Carr, J. S., & Graham, J. R. 2011, *ApJ*, submitted

Dutrey, A., Guilloteau, S., & Guelin, M. 1997, *A&A*, **317**, L55

Dutrey, A., Guilloteau, S., & Ho, P. 2007, in *Protostars and Planets V*, ed. B. Reipurth, D. Jewitt, & K. Keil (Tucson, AZ: Univ. Arizona Press), 495

Eisner, J. A., Hillenbrand, L. A., White, R. J., Bloom, J. S., Akeson, R. L., & Blake, C. H. 2007, *ApJ*, **669**, 1072

Evans, N. J., II, et al. 2003, *PASP*, **115**, 965

Fischer, J., Gamache, R. R., Goldman, A., Rothman, L. S., & Perrin, A. 2003, *J. Quant. Spectrosc. Radiat. Transfer*, **82**, 401

Furlan, E., et al. 2006, *ApJS*, **165**, 568

Giannini, T., Nisini, B., & Lorenzetti, D. 2001, *ApJ*, **555**, 40

Gibb, E. L., Van Brunt, K. A., Brittain, S. D., & Rettig, T. W. 2007, *ApJ*, **660**, 1572

Gibb, E. L., Van Brunt, K. A., Brittain, S. D., & Rettig, T. W. 2008, *ApJ*, **686**, 748

Glassgold, A. E., Meijerink, R., & Najita, J. R. 2009, *ApJ*, **701**, 142

Glassgold, A. E., Najita, J., & Igea, J. 2004, *ApJ*, **615**, 972

Greene, T. P., & Lada, C. J. 1996, *AJ*, **112**, 2184

Guedel, M., et al. 2010, *A&A*, **519**, 113

Gullbring, E., Hartmann, L., Briceno, C., & Calvet, N. 1998, *ApJ*, **492**, 323

Hamann, F., & Persson, S. E. 1992, *ApJ*, **394**, 628

Harich, S. A., Hwang, D. W. H., Yang, X., Lin, J. J., Yang, X., & Dixon, R. N. 2000, *J. Chem. Phys.*, **113**, 10073

Harris, G. J., Tennyson, J., Kaminsky, B. M., Pavlenko, Ya. V., & Jones, H. R. A. 2006, *MNRAS*, **367**, 400

Hartigan, P., Edwards, S., & Ghandour, L. 1995, *ApJ*, **452**, 736

Hartigan, P., & Kenyon, S. J. 2003, *ApJ*, **583**, 334

Hartmann, L., Calvet, N., Gullbring, E., & D'Alessio, P. 1998, *ApJ*, **495**, 385

Herbst, E., & van Dishoeck, E. F. 2009, *ARA&A*, **47**, 427

Houck, J. R., et al. 2004, *ApJS*, **154**, 18

Jaeger, C., Molster, F. J., Dorschner, J., Henning, Th., Mutschke, H., & Waters, L. B. F. M. 1998, *A&A*, **339**, 904

Jørgensen, J. K., Schoier, F. L., & van Dishoeck, E. F. 2004, *A&A*, **416**, 603

Knez, C., et al. 2007, *BAAS*, **211**, 5005

Kruger, A. J., Richter, M. J., Carr, J. S., Najita, J. R., Doppmann, G. W., & Seifahrt, A. 2011, *ApJ*, **729**, 145

Lahuis, F., & van Dishoeck, E. F. 2000, *A&A*, **355**, 699

Lahuis, F., et al. 2006a, *ApJ*, **636**, L145

Lahuis, F., et al. 2006b, C2d Spectroscopy Explanatory Supplement (Pasadena, CA: Spitzer Science Center)

Mandell, A. M., Mumma, M. J., Blake, G. A., Bonev, B. P., Villanueva, G. L., & Salyk, C. 2008, *ApJ*, **681**, L25

McCabe, C., Ghez, A. M., Prato, L., Duchêne, G., Fisher, R. S., & Telesco, C. 2006, *ApJ*, **636**, 932

Meijerink, R., Pontoppidan, K. M., Blake, G. A., Poelman, D. R., & Dullemond, C. P. 2009, *ApJ*, **704**, 1471

Melnick, G. J., Tolls, V., Neufeld, D. A., Yuan, Y., Sonnentrucker, P., Watson, D. M., Bergin, E. A., & Kaufman, M. J. 2008, *ApJ*, **683**, 876

Najita, J. R., Carr, J. S., Glassgold, A. E., & Valenti, J. A. 2007a, in *Protostars and Planets V*, ed. B. Reipurth, D. Jewitt, & K. Keil (Tucson, AZ: Univ. Arizona Press), 507

Najita, J. R., Carr, J. S., & Mathieu, R. D. 2003, *ApJ*, **589**, 913

Najita, J. R., Carr, J. S., Strom, S. E., Watson, D. M., Pascucci, I., Hollenbach, D., Gorti, U., & Keller, L. 2010, *ApJ*, **712**, 274

Najita, J. R., Doppmann, G. W., Carr, J. S., Graham, J. R., & Eisner, J. A. 2009, *ApJ*, **691**, 738

Najita, J. R., Edwards, S., Basri, G., & Carr, J. 2000, in *Protostars and Planets IV*, ed. V. Mannings, A. P. Boss, & S. S. Russell (Tucson, AZ: Univ. Arizona Press), 457

Najita, J. R., Strom, S. E., & Muzerolle, J. 2007b, *MNRAS*, **378**, 369

Neufeld, D. A., et al. 2009, *ApJ*, **706**, 170

Nisini, B., et al. 2010, *A&A*, **518**, L120

Nomura, H., Aikawa, Y., Tsujimoto, M., Nakagawa, Y., & Millar, T. J. 2007, *ApJ*, **661**, 334

Pascucci, I., Apai, D., Luhman, K., Henning, Th., Bouwman, J., Meyer, M. R., Lahuis, F., & Natta, A. 2009, *ApJ*, **696**, 143

Pontoppidan, K. M., Salyk, C., Blake, G. A., & Kaufl, H. K. 2010a, *ApJ*, **722**, L173

Pontoppidan, K. M., Salyk, C., Blake, G. A., Meijerink, R., Carr, J. S., & Najita, J. 2010b, *ApJ*, **720**, 887

Pontoppidan, K. M., et al. 2008, *ApJ*, **678**, 1005

Prato, L., Greene, T. P., & Simon, M. 2003, *ApJ*, **584**, 853

Rothman, L. S., et al. 2005, *J. Quant. Spectrosc. Radiat. Transfer*, **96**, 139

Salyk, C., Pontoppidan, K. M., Blake, G. A., Lahuis, F., van Dishoeck, E. F., & Evans, N. J., II. 2008, *ApJ*, **676**, L49

Salyk, C., Pontoppidan, K. M., Blake, G. A., Najita, J. R., & Carr, J. C. 2011, *ApJ*, **731**, 130

Skemer, A. J., Close, L. M., Hinz, P. M., Hoffmann, W. F., Greene, T. P., Males, J. R., & Beck, T. L. 2010, *ApJ*, **711**, 1280

Tappe, A., Lada, C. J., Black, J. H., & Muench, A. A. 2008, *ApJ*, **680**, L117

Thi, W.-F., van Zadelhoff, G.-J., & van Dishoeck, E. F. 2004, *A&A*, **425**, 955

Willacy, K., & Woods, P. M. 2009, *ApJ*, **703**, 479

Woitke, P., Kamp, I., & Thi, W.-F. 2009, *A&A*, **501**, 383